



Large eddy simulation of the flow around a high-rise building with special focus on the two-points two-times second order statistics of the velocity field

Mohanad Elagamy ^{a,*}, Nishchay Tiwari ^b, Cristobal Gallego-Castillo ^a, Alvaro Cuerva-Tejero ^a, Oscar Lopez-Garcia ^a, Sergio Avila-Sanchez ^a

^a Aircraft and Space Vehicles Department, Universidad Politécnica de Madrid, Plaza Cardenal Cisneros 3, 28040, Madrid, Spain

^b Institute of Fluid-Flow Machinery, Polish Academy of Sciences, Fiszera 14, Gdańsk, 80-231, Poland

ARTICLE INFO

Keywords:

Turbulence
Urban wind energy
High rise building
Numeric generation
Spectral representation method
Large-eddy simulation

ABSTRACT

Comprehending the wind characteristics in urban environments is crucial to ensure optimal performance and structural integrity of wind turbines operating in urban areas. This study aims to provide a deeper insight into wind characteristics over high-rise buildings rooftop. The impact of a high-rise building configuration on the turbulent wind field characteristics is analyzed, by means of large eddy simulations of a reference wind tunnel experiment. Special attention is paid to the analysis of the second order statistics of the turbulent velocity components, as they are crucial inputs for generating synthetic urban wind fields for wind turbine aeroelastic simulations. A Spectral Representation Method is applied to generate the desired turbulent inflow represented in the experiment study. The correspondence between the predicted statistics and the experimental values of the velocity components over the rooftop reinforces the idea about the practical viability of large eddy simulation to provide atmospheric turbulence information in the urban environment required to characterize the behavior of wind systems operating in that environment. Additionally, the two-points two-times second order statistics are significantly affected by the presence of the high-rise building, especially when those statistics involve at least a point within the recirculation bubble region.

1. Introduction

The global climate crisis urges us to rapidly replace fossil energy sources with renewable sources. This requires massive installation of renewable capacity. In this context, urban environment has several advantages connected with distributed renewable generation. Small wind turbine (SWT) technology is gaining popularity as it reduces some of the barriers associated with large-scale wind farms (Musial and Ram, 2010). However, the insufficient comprehension of the wind field characteristics in urban areas resulted in inadequate safety measures for the SWTs and poor performance (Smith et al., 2012; KC et al., 2019). The characteristics of wind flows in the built environment is rather different than the flow field developed over flat and open terrains (Kaimal and Finnigan, 1994) since the local airflow patterns are significantly influenced by the non-homogeneous roughness of the urban area (Ricciardelli and Polimeno, 2006). Understanding the flow characteristics in urban areas is crucial to ensure the safety of the SWT structure and improve its performance (Stathopoulos et al., 2018).

The SWTs must be tested under the wind conditions defined by International Electrotechnical Commission (IEC) (IEC 61400-2, 2019) standards. The IEC 61400-2 provides a description of the mean velocity

and the turbulence intensity using the normal turbulence model, which are used for the aeroelastic simulations of SWT mounted over building roofs. However, this description is based on data obtained for open and flat terrains. Therefore, this could lead to ill-prediction of the dynamic loads on the SWT as urban airflows are characterized by high levels of turbulence and frequent variations in wind direction (Nelson et al., 2004; Eliasson et al., 2006; Ricciardelli and Polimeno, 2006; Nelson et al., 2007b,a).

Both, experimental and numerical approaches can contribute to the comprehension of the wind field characteristics in built environments, with enough fidelity as to be useful in the characterization of wind energy systems operating in such environments. The Architectural Institute of Japan (AIJ, 2007) and the Compilation of Experimental Data for Validation of microscale dispersion models (CEDVAL, 2006) provide numerical and experimental data for understanding wind flows around a single building or clusters of buildings. It is worth mentioning that these studies are primarily focused on the evaluation of wind conditions at the pedestrian level. Field measurements were performed in Oklahoma City in the United States, wherein measurements were

* Corresponding author.

E-mail address: mohanad.elagamy@upm.es (M. Elagamy).

taken at various locations within the city, both at the pedestrian and building level (Nelson et al., 2004, 2007b,a). The aim of these field measurements was to understand the wind patterns over an urban area and how they are influenced by wind direction variations. Fortuniak and Pawlak (2015) analyzed the spectra of wind velocity components over Łódź in Poland. Fortuniak and Pawlak (2015) showed that the spectra of urban wind field have similar characteristics to the spectra of wind field over a homogeneous flat terrain described by Kaimal et al. (1972). However, some features such as peaks can appear in the spectra of urban wind field due to characteristic phenomena (Nelson et al., 2007b; Vita et al., 2020c), such as conical vortex, which takes place in built environment. Furthermore, Tabrizi et al. (2015) analyzed the influence of wind direction on spectra at the rooftop of a warehouse. Also, Christen et al. (2007) showed to what extent the integral length scales of the velocity components are affected by the presence of buildings. Additional research on understanding the urban wind field using wind tunnel and field measurements can be found in Brook (1972), Rotach (1991), Feigenwinter et al. (1999), Roth (2000), Christen et al. (2007) and Peng et al. (2020).

Various researchers have used the numerical approach such as Computational Fluid Dynamics (CFD) to understand the urban airflow at the rooftop of buildings. Micallef and Van Bussel (2018), Stathopoulos et al. (2018), Toja-Silva et al. (2018) and KC et al. (2019) provide detailed reviews of these studies. Abohela et al. (2013) examined the influence of building height, urban configuration as well as the shape of the rooftop on the wind flow characteristics over the rooftop. Toja-Silva et al. (2015) studied the impact of the roof shapes on the turbulence intensity and mean velocity over a building roof. The investigations conducted by the previous studies were done by utilizing Reynolds-averaged Navier-Stokes (RANS) approach, which can give a useful information of the mean wind field statistics (Vita, 2020). However, for a deeper understanding of the urban wind field characteristics, including two-points-two times second order statistics, as well as having more accurate and reliable results, advanced numerical methods such as Large Eddy Simulations (LES) are required (Blocken, 2015, 2018). There are studies that have utilized LES for simulating wind field over built environment, although their primary focus has been on characterizing the dispersion of pollutants (Merlier et al., 2019) and assessing pedestrian comfort (Tolias et al., 2018; Jacob and Sagaut, 2018). Kono et al. (2016) investigate the wind condition over the rooftop of isolated buildings, analyzing the effect of wind direction and horizontal aspect ratio of a building on the wind resources at the rooftop. However, a full description of the wind field characteristics, providing second-order statistics such as the spectra and covariance, at the rooftop was not presented.

Most of the mentioned studies offer limited information about the wind flow characteristics at the rooftop. In particular, they lack of providing a more comprehensive description of the spatial variation description of the second-order statistics of the wind velocity components, either in the frequency domain (cross-spectra) or in the time domain (cross-covariances), including the spectra at different height levels and/or spatial coherence of the wind field, which is essential as they are driving factor of the wind turbine loading (Dimitrov et al., 2017). To fill that research gap, Šarkić-Glumac et al. (2018a), Hemida et al. (2020) and Vita et al. (2020c) performed wind tunnel experiments to analyze the wind flow over the rooftop of a single building and over a group of buildings. Moreover, they investigated the impact of different rooftop shapes and the effect of changing the wind direction on the wind characteristics. Hemida et al. (2020) analyzed the velocity and pressure fields over the isolated building, whilst Šarkić-Glumac et al. (2018a) focused on the cluster effect. Vita et al. (2020c) provided a more comprehensive description of the wind velocity field at potential rooftop locations for the SWT, which was also compared with a LES simulation done by Vita (2020). Furthermore, Vranešević et al. (2022) utilized LES simulations to characterize the flow pattern around the isolated building configuration and compared the results

with experimental measurements provided by Šarkić-Glumac et al. (2018a), Hemida et al. (2020) and Vita et al. (2020c).

This study builds upon the prior studies done by Šarkić-Glumac et al. (2018a), Hemida et al. (2020) and Vita et al. (2020c), where LES is utilized to gain a deeper understanding of the wind flow over an isolated building. The main research question is how does LES of highly non-homogeneous flows provide promising estimations of two-points two-times second order statistics of velocity fields, useful for (a) characterizing wind loading in future locations of systems operating on HRB and (b) serving as deterministic input data for synthesizing velocity fields using numerical generation methods. Properly characterizing the two-points two-times second order statistics of the velocity components from LES is crucial to the synthesis process, as they serve as the main inputs for various numerical generation methods such as Spectral Representation Methods (SRM) (Veers, 1988; Mann, 1998) and Sequential Methods (SM) (Krenk and Møller, 2019; Gallego-Castillo et al., 2021; Elagamy et al., 2023). Accurately resolving these statistics leads to a better representation of the turbulence in the synthetic wind field and enhances the prediction of loads acting on the SWT in complex urban environments.

With this main question in mind, the contribution of the present work can be divided into two key parts. In the first part, a validation is performed by comparing first-order statistics (means), second-order statistics (variances), and second-order one-point statistics (cross-spectra at a single point) with reference experimental and reference LES data. The second part investigates two potential locations for a hypothetical SWT by analyzing second-order one-point statistics, such as the spectra and autocovariance of wind velocity components, at various points along a vertical line above the rooftop. This analysis includes the spatial coherence of velocity components as representative of relevant two-points two-times second order statistics and examining the wind field characteristics over a vertical plane perpendicular to the mean wind velocity, which represents the rotor plane of the hypothetical SWT. Additionally, a comparison of the wind field characteristics with and without the presence of the HRB is provided. This comparison is relevant because current urban wind modeling standards, such as IEC 61400-2, rely on turbulence models like von Karman and Kaimal spectra, which provide simplified flow conditions not representative of urban wind fields.

The arrangement of sections in this article is as follows. In Section 2, preliminary definitions of the statistical characteristics of turbulent wind velocity are introduced. Section 3 provides details on the reference LES study and reference wind tunnel experiment that were replicated in this study. In Section 4, the Spectral Representation Method for synthetic generation of the turbulent wind inflow field at the domain inlet, based in the Mann's Uniform-Shear Spectral Velocity Tensor Model, is illustrated. The LES setup is presented in Section 4, including the process to select the Mann model parameters which produces a synthetic turbulence field at the domain inlet which gives rise to best match of the undisturbed inflow characteristics at the HRB location. Section 5 shows the assessment of the conducted LES simulation by comparing it to the reference experiment and LES simulations. In Section 6, the results on the two-points two-times second order statistics over the HRB rooftop are shown and analyzed. Finally, conclusions regarding the current study are derived in Section 7.

2. Preliminary definitions and notation

In this section, preliminary definitions of the statistical characteristics of wind field is introduced.

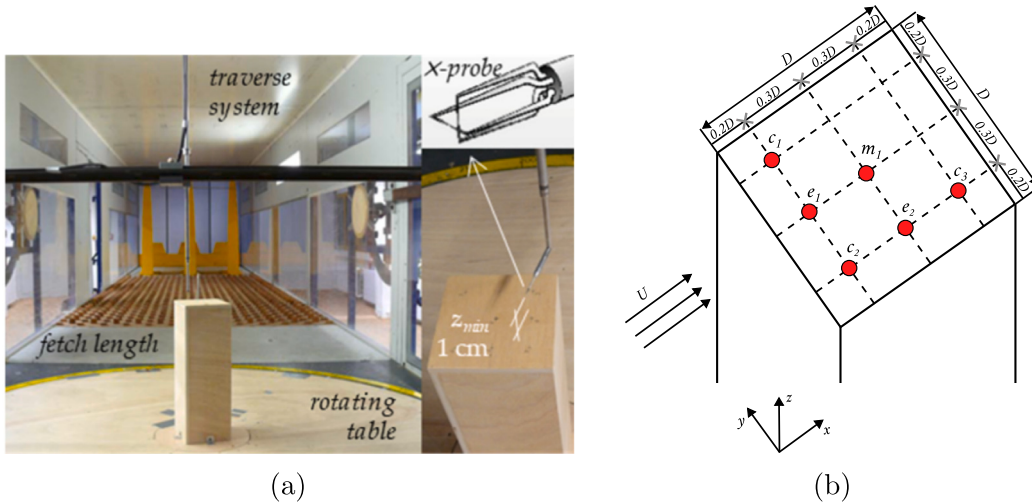


Fig. 1. (a) Wind tunnel in RUB with the building model (Vita, 2020) (figure acquired from (Vita et al., 2020c)) and (b) the locations of the measurements of the HWA on the rooftop.

2.1. Mean velocity and turbulence intensity

The wind velocity vector, $[\tilde{u}, \tilde{v}, \tilde{w}]^T$, where the superscript $(\cdot)^T$ stands for transpose, is expressed by Reynolds's decomposition (Pope, 2000):

$$\begin{bmatrix} \tilde{u} \\ \tilde{v} \\ \tilde{w} \end{bmatrix} = \begin{bmatrix} U \\ V \\ W \end{bmatrix} + \begin{bmatrix} u \\ v \\ w \end{bmatrix}, \quad (1)$$

where $[U, V, W]^T$ is the mean value (here considered as time average, i.e. statistical stationarity is considered) of the wind velocity vector, and $[u, v, w]^T$ is its fluctuation.

Additionally, the turbulence intensity of each velocity component, $I_i = \sqrt{\overline{i^2}}/S$, for $i = u, v, w$, is evaluated by dividing its variance, $\overline{i^2}$ (where the overline $\overline{(\cdot)}$ refers to time average), of the i -velocity component by the local mean wind speed defined as $S = \sqrt{U^2 + V^2 + W^2}$.

2.2. Integral length scales and autocovariance functions

The integral length scales in the x -direction, $L_i^x = ST_i$, are calculated from the corresponding integral time scales T_i and the application of the Taylor's Frozen Turbulence Hypothesis (TFTH) (Panofsky and Dutton, 1984; Kaimal and Finnigan, 1994). The integral time scale is defined as $T_i = \int_0^{\tau^*} \gamma_{ii}(\tau)/\overline{i^2} d\tau$, where τ is the time lag, τ^* is the upper limit of the integration and $\gamma_{ii}(\tau) = \overline{i(t)i(t+\tau)}$ is the temporal Autocovariance Function (ACF) of the i -velocity component fluctuation. The first zero-cross approach is considered to define τ^* , where τ^* is set to the time lag at which the ACF reaches its first zero value (Panofsky and Dutton, 1984; Emes et al., 2016).

2.3. Spatial coherence function and spectra

The spatial coherence, $coh_i(f, \Delta z)$, for $i = u, v, w$, in terms of the frequency f and a vertical separation distance Δz , is defined as (Burton et al., 2011):

$$coh_i(f, \Delta z) = \frac{|S_{i_A i_B}(f)|^2}{S_{i_A i_A}(f) S_{i_B i_B}(f)}, \quad (2)$$

where $S_{i_A i_A}$ and $S_{i_B i_B}$ are the auto-Power Spectral Density (PSD), $S_{i_A i_B}$ is the Cross-Power Spectral Density (CPSD), the sub-index $(\cdot)_A$ and $(\cdot)_B$ refer to the grid points at (x, y, z) and $(x, y, z + \Delta z)$, respectively.

3. Description of the reference LES and experimental database

This section briefly describes the reference wind tunnel experiment setup, which was carried out by Hemida and Šarkić (2014), Šarkić-Glumac et al. (2018a), Hemida et al. (2020) and Vita et al. (2020c). Additionally, it illustrates the setup of the reference LES simulations done by Vita (2020) and Vranešević et al. (2022), which were used as an assessment for the LES simulation done in the present work.

3.1. Wind tunnel experiments database

Wind tunnel experiments were conducted by Hemida and Šarkić (2014), Šarkić-Glumac et al. (2018a), Hemida et al. (2020) and Vita et al. (2020c), with the aim to study the wind flow over the rooftop HRBs. In the present work, only the wind direction perpendicular to the windward face of the building is considered. The experimental data may be accessed as Mendelay Data in Šarkić-Glumac et al. (2018b) and Šarkić-Glumac et al. (2020). Fig. 1(a) shows the model of the single HRB along with the Hot-Wire Anemometer (HWA) and the traverse system, which is used to take measurements above the rooftop. The HWA is employed for measuring the u and w -velocity components. It is noteworthy that the probe was unable to account for reverse flow (Vita et al., 2020c; Vita, 2020). The building model has a height $H = 0.4$ m and a width $D = H/3 \approx 0.13$ m. In Fig. 1(b), the measurement locations at the rooftop are depicted. The six considered locations are the middle of the rooftop (m_1), the windward and leeward corners (c_1, c_2, c_3), and the edges of the windward and leeward (e_1, e_2). All data for the reference cases were extracted using a digitizing tool. Based on the extracted data, the estimated measurement heights at locations e_1 and m_1 are given by $z^*/D = 0.075 \cdot i$ where $i = 1, 2, \dots, 10$. At locations e_2 , c_1 , c_2 , and c_3 , the heights are $z^*/D = 0.075 \cdot \{1, 4, 6\}$.

The turbulent inflow generated upstream of the model in the wind tunnel by a long fetch equipped with wood blocks (see Fig. 1(a)) fits the power law profile,

$$U(z) = U_{ref} \left(\frac{z}{z_{ref}} \right)^\alpha, \quad (3)$$

with exponent $\alpha = 0.2$ and a reference velocity $U_{ref} = 16 \text{ m s}^{-1}$ at the reference height $z_{ref} = H$. The turbulent inflow generated is in accordance with Eurocodes-defined terrain category II (Eurocode, 2005; Vita et al., 2020c). Fig. 2 shows the non-dimensional mean wind longitudinal velocity profile, U/U_{ref} of the conducted LES simulation together with the corresponding from the reference experiment and the power law profile. Additionally, the longitudinal and vertical turbulence intensities, I_u and I_w are also shown with their corresponding

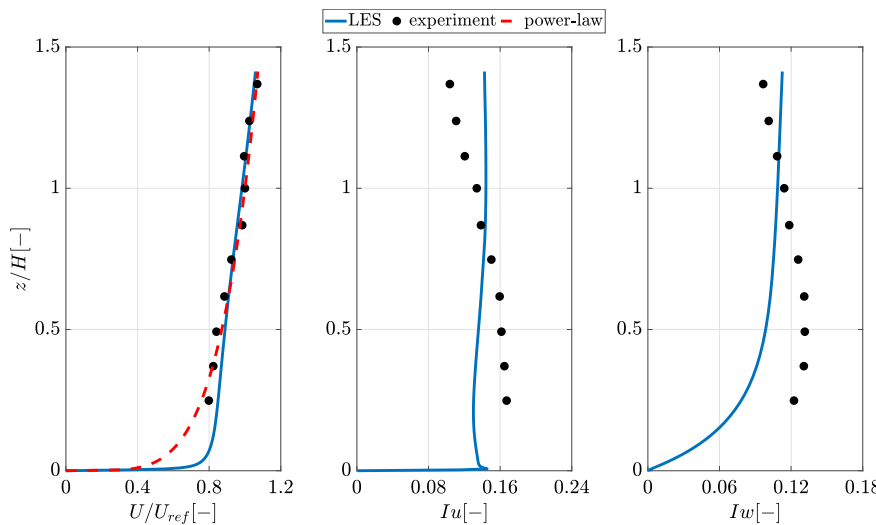


Fig. 2. Comparison of the turbulent inflow generated by the LES performed in the current study, the experiment turbulent inflow and the power law. [left] the non-dimensional mean speed profile, U/U_{ref} , [middle] the longitudinal turbulence intensity, I_u , and [right] the vertical turbulence intensity, I_w .

experimental values. Further information about the wind tunnel experiment can be found in Hemida and Šarkić (2014), Šarkić-Glumac et al. (2018a), Hemida et al. (2020) and Vita et al. (2020c). The Reynolds number based on the building width D is equal to

$$\text{Re} = DU_{ref}/\nu_{air} = 1.4 \times 10^5.$$

3.2. LES simulations database

In addition to the wind tunnel experiments, LES simulations were conducted in OpenFOAM by Vita (2020) and Vranešević et al. (2022), modeling a virtual wind tunnel similar to the wind tunnel of RUB. The turbulent inlet in the LES simulations was generated with roughness cubes and barriers at the inlet of the computational domain. Vita (2020) used the Smagorinsky-Lilly model (Smagorinsky, 1963; Lilly, 1962) as the Sub-Grid Scale (SGS) model in the LES simulation, whereas, Vranešević et al. (2022) used the Wall-Adapting Local Eddy-viscosity (WALE) model (Nicoud and Ducros, 1999). Note that in the following sections, these reference LES simulations will be referred to them as LES-Vita and LES-Vranešević. The results from both reference LES simulations for the e_1 and m_1 locations at the rooftop were used to assess the LES simulation done in the present work.

4. Numerical methodologies

4.1. Governing equations

The LES governing equations are derived through spatial filtering of the incompressible Navier–Stokes (N–S) equations as follows (Pope, 2000; Wyngaard, 2010):

$$\begin{aligned} \frac{\partial \tilde{u}_i^r}{\partial x_i} &= 0, \\ \frac{\partial}{\partial t} (\tilde{u}_i^r) + \frac{\partial}{\partial x_j} (\tilde{u}_i^r \tilde{u}_j^r) &= \nu \frac{\partial^2 \tilde{u}_i^r}{\partial x_j \partial x_j} - \frac{1}{\rho} \frac{\partial \tilde{p}^r}{\partial x_i} - \frac{\partial \tau_{ij}}{\partial x_j}, \end{aligned} \quad (4)$$

where \tilde{u}_i^r is the filtered velocity component in the direction x_i (for $i = 1, 2, 3$), t is the time coordinate, \tilde{p}^r is the filtered pressure, ν and ρ are the kinematic viscosity and the air density, respectively and τ_{ij} is the SGS stress tensor. Note that the superscript $(\cdot)^r$ refers to the resolved-scale quantity after spatial filtering. The present work uses the WALE model (Nicoud and Ducros, 1999) has been used to evaluate the SGS tensor due to its capability to capture the near-wall behavior of

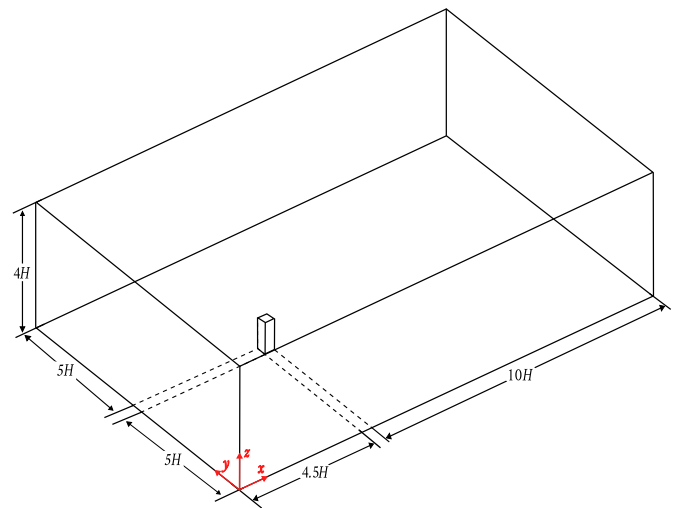


Fig. 3. Scheme of the computational domain with a representation of the HRB of height H and width D .

turbulent flows more accurately. Furthermore, the PIMPLE algorithm is used for the pressure–velocity coupling (Patankar and Spalding, 1972; Issa, 1986).

4.2. Simulation setup

The computational domain utilized in the presented LES simulation is shown in Fig. 3. The domain was selected according to the guidelines provided by the European Cooperation in Science and Technology (Franke et al., 2007) and the AIJ (Tominaga et al., 2008). The inlet boundary is selected to be $4.5H$ upstream of the building and the outlet boundary is set to be $10H$ downstream of the building. The lateral boundaries are set to be $5H$ away from the building and the top boundary is set at a height of $4H$. The Blockage Ratio (BR) of the selected computational domain is

$$\text{BR} (\%) = \frac{H \times D}{\text{domain cross section}} = 0.81\%,$$

which is in agreement with the guidelines provided in Tominaga et al. (2008).

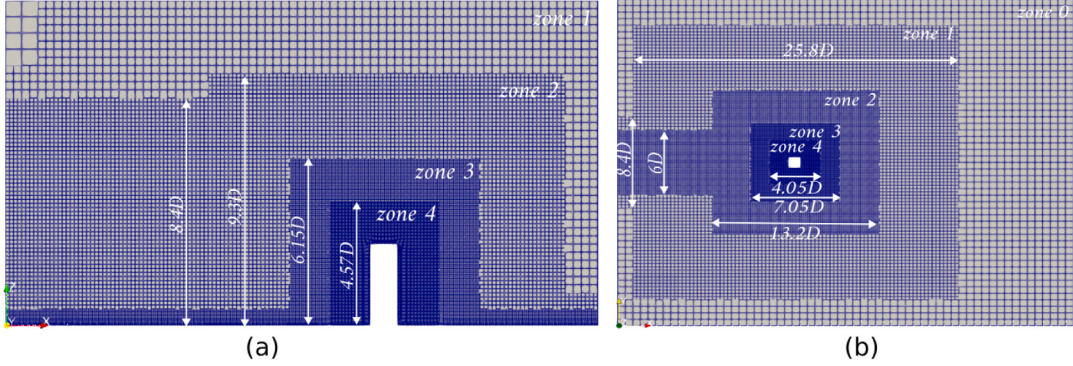


Fig. 4. Visualization of the mesh domain which close to the HRB showing (a) the side view, and (b) the top view.

Table 1

Main parameters of the numerical setup. Δ_0 is the primary mesh layer's thickness on the building surface.

	Case I (fine)	Case II (coarse)	Case II (intermediate)	Case II (fine)
Refinement levels	3	3	3	4
Δt (s)	2.5×10^{-5}	2.5×10^{-5}	2.5×10^{-5}	2.5×10^{-5}
$\Delta x_{\min}/D$	3.75×10^{-2}	6.25×10^{-2}	4.69×10^{-2}	3.75×10^{-2}
$\Delta x_{\max}/D$	0.6	0.6	0.6	0.6
Δ_0/D	1.9×10^{-3}	3×10^{-3}	1.5×10^{-3}	7.5×10^{-4}
Number of cells	6,018,108	2,468,718	4,058,145	6,718,696

The simulated synthetic wind field defined, generated by Mann's approach (described in Sections 4.3 and 4.4), is prescribed at the inlet boundary. No-slip boundary conditions are applied at ground level and on all building surfaces. While zero-gradient conditions are imposed on the top boundary. The boundary condition used at the outlet is called inletOutlet which sets the patch value to the fixed value in case of the reversed flow and treats the patch as the zero gradient condition in case of outflow. Moreover, periodic boundary conditions are set on boundaries in the spanwise directions.

In the present work, the aim is to analyze the statistical characteristics of the wind flow over the rooftop without (case I) and with the building (case II). The Numeca Hexpress tool was utilized to generate hexahedral unstructured mesh. The computational domain was discretized using embedded subdomains of hexahedral cells that maintain a constant ratio of two between successive subdomains. The finer mesh near the building was created using block refinement which is followed by a refinement diffusion, which is less dissipating and is required for the transport of turbulent flow. A scheme of the subdomains mesh for the fine grid, for case II, is depicted in Fig. 4. The size of the smallest and the largest cells for the fine grid is $\Delta x_{\min}/D = 3.75 \times 10^{-2}$ and $\Delta x_{\max}/D = 0.6$ for both case I and II. Moreover, the number of cells for the fine grid is ~ 6 million and ~ 6.7 million for case I and case II, respectively. For the fine grid simulation, an average value of $y^+ \sim 2$ over the surface of the building is obtained. In Table 1, the mesh grid parameters are summarized. Furthermore, the mesh dependence study is shown in Appendix. The simulation time (T) is 65 s. The time scale for the large turbulent structures generated by the HRB is estimated as $H/U_{ref} = 0.025$ s, resulting in a normalized simulation time of $T U_{ref}/H = 2600$. The time interval used for flow statistics determination is $(T - 1) U_{ref}/H = 2560$, which is significantly larger than the estimated eddy turnover time.

4.3. Spectral representation method for inlet turbulence synthetic generation

The approach proposed by Mann (1998) was applied to generate synthetic turbulent fluctuations for the \tilde{u} , \tilde{v} and \tilde{w} velocity components to be used as turbulent velocity field at the inlet of the domain. The synthetic wind field was generated by utilizing the MATLAB code "MannTurb4D_v1 (Version v1.0)" developed by Guo and Mann (2022).

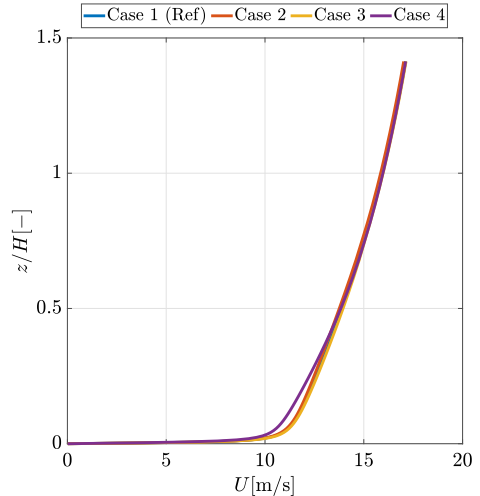


Fig. 5. The mean wind longitudinal velocity profile of the simulated wind field at the mid-plane of the empty domain, for the considered cases (see Table 2).

In Mann's approach, a stochastic process representing the fluctuation of the wind velocity vector field, $u_i(\mathbf{x}_\perp, t; \alpha)$, for each velocity component $i = 1, 2, 3$, is obtained from a purely spatial stochastic process defined on a computational domain with dimension $L_x \times L_y \times L_z$. The L_x is discretized into N_x spatial intervals. The fluctuation field $u_i(\mathbf{x}_\perp, t; \alpha)$ of each realization, α , is obtained by applying TFTH as follows:

$$u_i(\mathbf{x}_\perp, t; \alpha) = u_i(\mathbf{x}_\perp - tU\mathbf{i}, 0; \alpha), \quad (5)$$

and the spatial-discrete stochastic process $u_i(\mathbf{x}_\perp, 0; \alpha)$ is expressed as:

$$u_i(\mathbf{x}_\perp, 0; \alpha) = \sum_{k_1} \sum_{k_2} \sum_{k_3} U_{ij}(k) n_j(k, \alpha) \exp(i\mathbf{k}^T \mathbf{x}), \quad (6)$$

where $j = 1, 2, 3$, $\mathbf{k} = [k_1, k_2, k_3]^T$ is the wavenumber vector, $i = \sqrt{-1}$ is the imaginary unit and $n_j(k, \alpha)$ are the independent Gaussian stochastic complex variables with unit variance. The deterministic coefficient

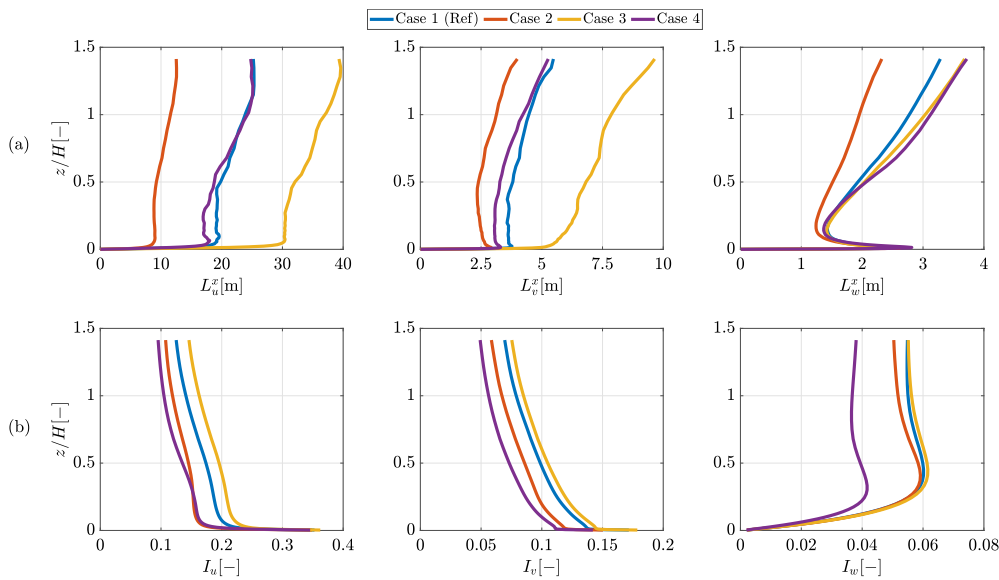


Fig. 6. Vertical profiles of (a) Integral length scales along the x direction, and (b) the turbulence intensity, for the u, v and w velocity components at the mid-plane of the empty domain, for the four considered synthetic inlets (see Table 2).

matrix $U_{ij}(\mathbf{k})$, in expression (6), can be related to the Spectral Velocity Tensor (SVT), $\Phi_{ij}(\mathbf{k})$ as (Mann, 1998):

$$U_{ik}^*(\mathbf{k})U_{jk}(\mathbf{k}) = \frac{2\pi}{L_x L_y L_z} \Phi_{ij}(\mathbf{k}), \quad (7)$$

where the superscript $(\cdot)^*$ refers to complex conjugate. The SVT, used in Eq. (7), is evaluated from the Mann Uniform-Shear SVT (US-SVT), $\Phi_{ij}(\mathbf{k})$, Mann (1994, 1998), which reproduces the second order statistics of a stationary-homogeneous-anisotropic turbulence velocity field. The Mann's US-SVT model is affected by anisotropy parameter Γ ($\Gamma = 0$ means isotropy), the length scale of the energy spectrum L and an isotropic variance u_{iso}^2 which is defined as:

$$\overline{u_{iso}^2} = \iiint_k \Phi_{ij}(\mathbf{k}) \Big|_{\Gamma=0} d\mathbf{k}. \quad (8)$$

4.4. Parametric study for synthetic generation of turbulent inflow for LES simulation

To replicate the inlet flow for the HRB simulation, a parametric study was conducted by changing the values of (L , Γ and u_{iso}^2) of the Mann turbulence model, to generate a synthetic wind field fluctuation, by using Mann's approach (Mann, 1994, 1998). Subsequently, the mean value of the longitudinal velocity component represented by the power law profile, shown in Eq. (3), is added to the generated synthetic wind velocity vector fluctuation field. The generated synthetic wind field is prescribed as turbulent inflow for an LES simulation for an empty domain with dimensions matching those of the main simulation and employing the same boundary conditions. Furthermore, a mesh with a number of cells ~ 2 million was used for simulating the empty domain. The mean velocity profile and the turbulence intensity of the wind field at the mid-plane of the empty domain were analyzed, and compared to the provided experimental results for the turbulent inlet flow. Four combinations of the Mann's model parameters, presented in Table 2 have been considered. To investigate the impact of Mann's parameters, a reference case (Case 1) is established, to compare the other cases.

Figs. 5 and 6 show the vertical profiles of the mean wind longitudinal velocity, turbulence intensities, and integral length scales of the simulated wind field at the mid-plane of the empty domain, for the mentioned four combinations of Mann's model parameters. From Fig. 5, it is evident that the four different combinations of Mann's parameters do not have a relevant impact on the mean velocity vertical

profiles. Whereas, the turbulence intensities and integral length scales are clearly dependent of the considered combination of parameters. For cases 1 and 2, a variation in the length scale, L , was introduced while maintaining the other parameters constant. For the integral length scale profiles, a decrease in the L parameter causes a reduction in the integral length scale profiles for all three directions, as depicted in Fig. 6a. Whilst, for the turbulence intensities profiles, It was observed that a decrease in the L value leads to a reduction in the I_u and I_v profiles, with only a minor reduction observed in the I_w profile at high heights, as shown in Fig. 6b.

To investigate the influence of the anisotropy parameter, Γ , for case 1 and case 3, the Γ value was changed while keeping all other parameters constant. It was observed that increasing the value of Γ has a noticeable effect on the I_u profile, which increases with a higher Γ value, as shown in Fig. 6b. However, the I_v experiences only a slight change, and the I_w profile is almost the same. With regards to the integral length scales, the L_u^x and L_v^x show a noticeable increase in their profiles, while the L_w^x displays a slight change only at high levels.

The impact of the u_{iso}^2 , on statistical characteristics of the extracted wind field, was investigated by varying its value while remaining the other parameters the same, for case 1 and case 4. As shown in Fig. 6b, a reduction in the u_{iso}^2 results in a decrease in the turbulence intensity profile for all three directions. Whereas, the integral length scales display a slight change with changing u_{iso}^2 , as depicted in Fig. 6b.

It can be concluded from the previous analysis that to replicate the turbulence intensity, especially I_w , of the desired turbulent inflow provided by the experiments (shown in Fig. 2), a high value of u_{iso}^2 is required. To facilitate the process of identifying the Mann parameters, a numerical predictor model has been developed. This predictor utilizes quadratic polynomials to predict the change of the turbulence intensity profiles at different heights with changing the Mann's parameters. These polynomials are obtained from fitting the turbulence intensity profiles obtained, for the considered LES results considered the synthetic inlets in Table 2. Finally, an optimization process was conducted to search for the Mann parameters, which lead to better replication of the turbulence intensities, I_u and I_w , of the turbulent undisturbed inflow provided by the experiments. The optimization process uses the predictor to forecast the turbulence intensity profiles and compare them to the desired profiles. Note that, only the turbulence intensity profiles were considered, since from the previous analysis it was observed that Mann's parameters have a negligible effect on the mean speed profile.

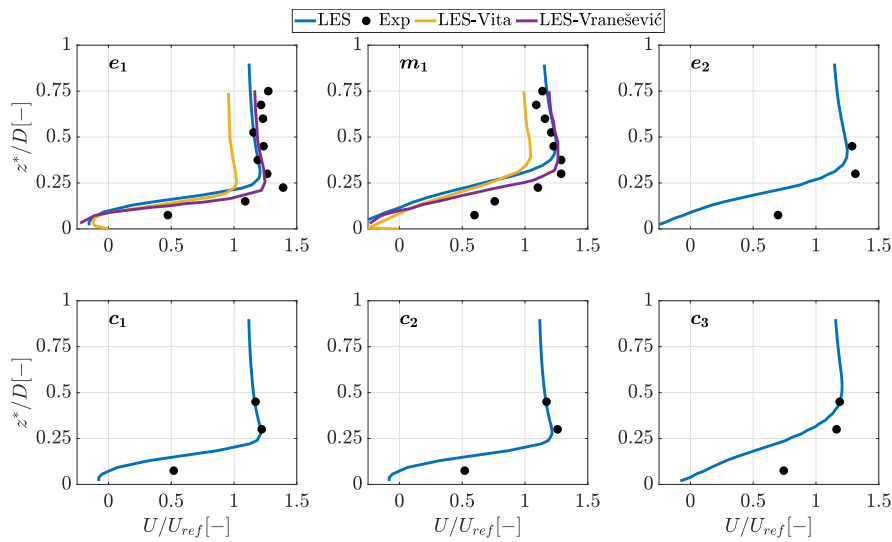


Fig. 7. Vertical profile of the non-dimensional mean longitudinal velocity component, U/U_{ref} , at different vertical lines over the rooftop locations shown in Fig. 1(b). In the figure, the results from the present LES analysis are represented as well as the results from the experimental data, LES-Vita and LES-Vranešević.

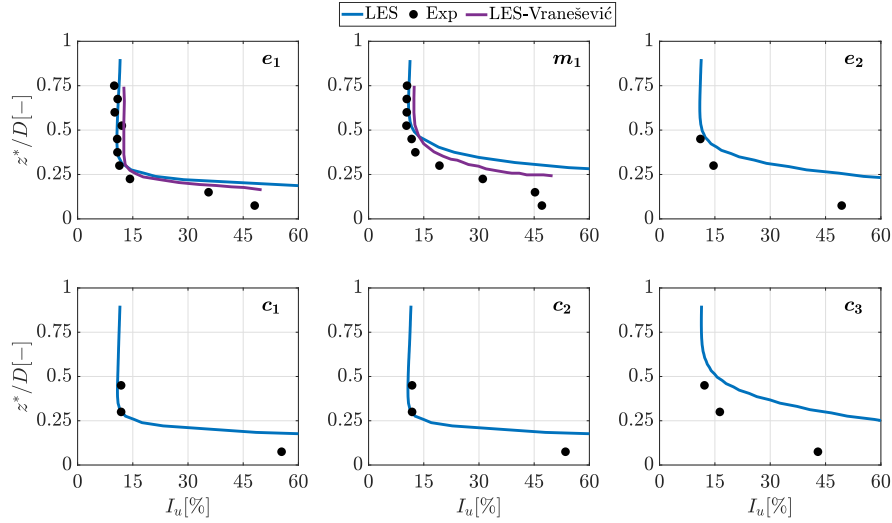


Fig. 8. Vertical profile of the longitudinal turbulence intensity, I_u , at different vertical lines over the rooftop locations shown in Fig. 1(b). In the figure, the results from the present LES analysis are represented as well as the results from the experimental data and LES-Vranešević.

Table 2

The four synthetic inlets prescribed in the empty domain inlet, considered in the parametric study to analyze the influence of the Mann's parameter on the generated wind field in the middle of the empty domain.

Cases	L (m)	$\overline{u_{iso}^2}$ ($\text{m}^2 \text{ s}^{-2}$)	Γ (-)
Case 1 (Ref)	0.5	2	2
Case 2	0.2	2	2
Case 3	0.5	2	3
Case 4	0.5	1	2

It is noteworthy that the increased number of turbulence profiles, generated by more LES runs, has led to a more precise and reliable prediction of the turbulence intensity, since the polynomials become more representative of the change of the turbulence intensity profiles with the change of the Mann's parameters.

The application of the predictor tool described above yielded to the following values for the Mann's model parameters: $\Gamma = 0$, $L = 0.25$ m and $\overline{u_{iso}^2} = 11 \text{ m}^2 \text{ s}^{-2}$. It must be noted that these parameters correspond to an unphysical flow, as the value of isotropic variance is

excessively high. However, utilizing the generated synthetic wind field as a turbulent inflow for the empty domain resulted in the attainment of a realistic wind field at the middle of the domain, which is consistent with the desired turbulent inflow as shown in Fig. 2. Subsequently, the wind field shown in Fig. 2 is used as the turbulent inflow to the main case, which includes the HRB. Note that the inflow turbulence characteristics play an important role in determining the flow behavior around surface-mounted obstacles, such as HRBs (Vita et al., 2020a,b). In this study, the inflow conditions used in the LES were designed to replicate those in the wind tunnel experiments, but some discrepancies remain, particularly in the turbulence intensity profiles above and below roof level, as shown in Fig. 2. A finer grid resolution or adjustments to the inflow parameters could improve the agreement between the LES and experimental data. It is worth mentioning that the inflow turbulence parameters, such as Reynolds number based on the height of the obstacle and the free wind speed at the obstacle height, the ratio of boundary layer thickness to obstacle height, inflow turbulence intensity, and the ratio of the inflow longitudinal length scale to the obstacle height can have a significant effect on the flow characteristics around surface-mounted obstacles (Yeow et al., 2011).

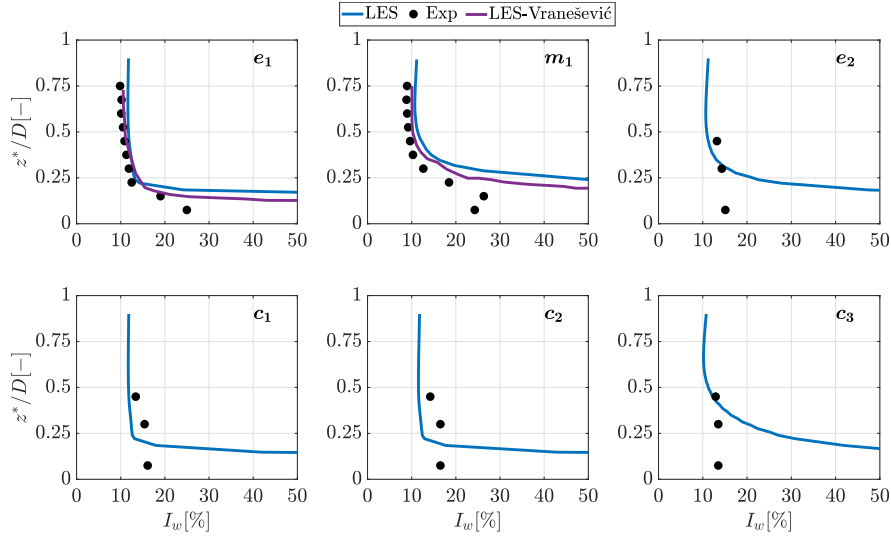


Fig. 9. Vertical profile of the vertical turbulence intensity, I_w , at different vertical lines over the rooftop locations shown in Fig. 1(b). In the figure, the results from the present LES analysis are represented as well as the results from the experimental data and LES-Vranešević.

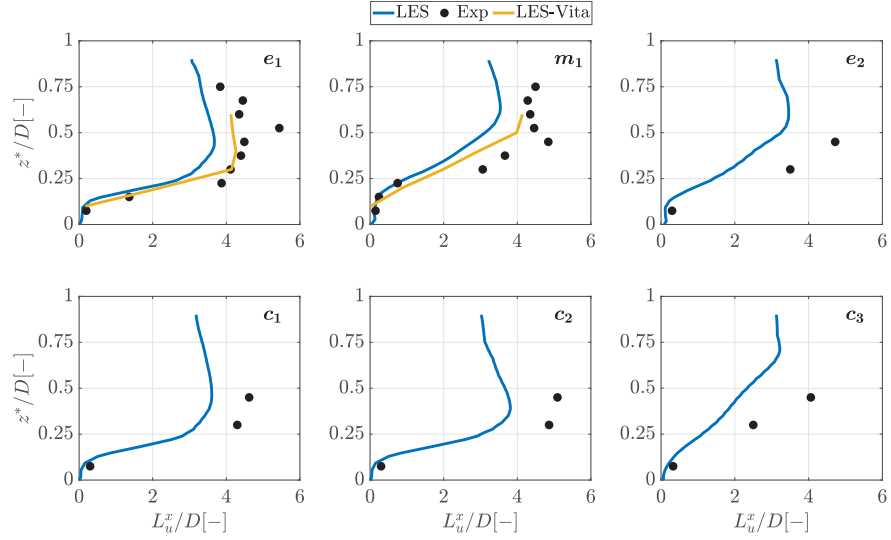


Fig. 10. Vertical profile of the non-dimensional longitudinal integral length scale, L_u^x/D , at different vertical lines over the rooftop locations shown in Fig. 1(b). In the figure, the results from the present LES analysis are represented as well as the results from the experimental data and LES-Vita.

These parameters influence the recirculation bubble properties, such as the longitudinal size of the bubble on the obstacle's surface. For instance, larger values of longitudinal turbulence intensity tend to reduce the length of the recirculation bubble, leading to a shorter reattachment length.

5. Assessment of the numerical approach

This section concerns the validation of the LES simulation defined in Section 4.2, by comparing its results with the reference cases. The statistical characteristics of the wind velocity field, at the rooftop locations shown in Fig. 1(b), are used for the comparison. Note that, although, the Δt used in the LES simulation is 2.5×10^{-5} s (see Table 1), the wind velocity field was saved for $\Delta t = 5 \times 10^{-4}$ s to decrease the memory requirement. The first second of the LES simulation was truncated to eliminate the initial transient part in the statistical calculations. In Fig. 7, the non-dimensional mean longitudinal velocity component, U/U_{ref} , along the non-dimensional height above the HRB rooftop, z^*/D (where $z^* = z - H$), is shown at various locations atop of the building. The results from the LES simulation display an agreement

with the experimental data and LES-Vranešević at high elevations. Note that the HWA is insensitive to reversed flow conditions, thus, the experimental results from the HWA are unreliable in the vicinity of the rooftop surface where flow recirculation is present due to the detachment bubble (Šarkić-Glumac et al., 2018a; Vita, 2020). The reversed flow close to the surface is well captured by the LES simulation. This reversed flow shows a level of consistency with the LES-Vita and LES-Vranešević for the rooftop locations e_1 and m_1 .

In Figs. 8 and 9 the longitudinal and vertical turbulence intensities I_u and I_w are shown at the validation locations. The I_u and I_w from the LES results exhibit a good agreement with the experimental results, particularly at high levels, however, some differences between the LES and the experimental results were noticed over the leeward side of the rooftop. This might be due to the increase in the reverse flow region thickness at the leeward side and most of the measuring points with the HWA are in the high turbulence intensity region, which might lead to inaccurate measurements from the HWA. Moreover, it is expected that the thickness of the high turbulence intensity region to be higher at the leeward edge of the building compared to the windward edge, which was observed in the DNS simulation in Yakhot et al. (2006). At

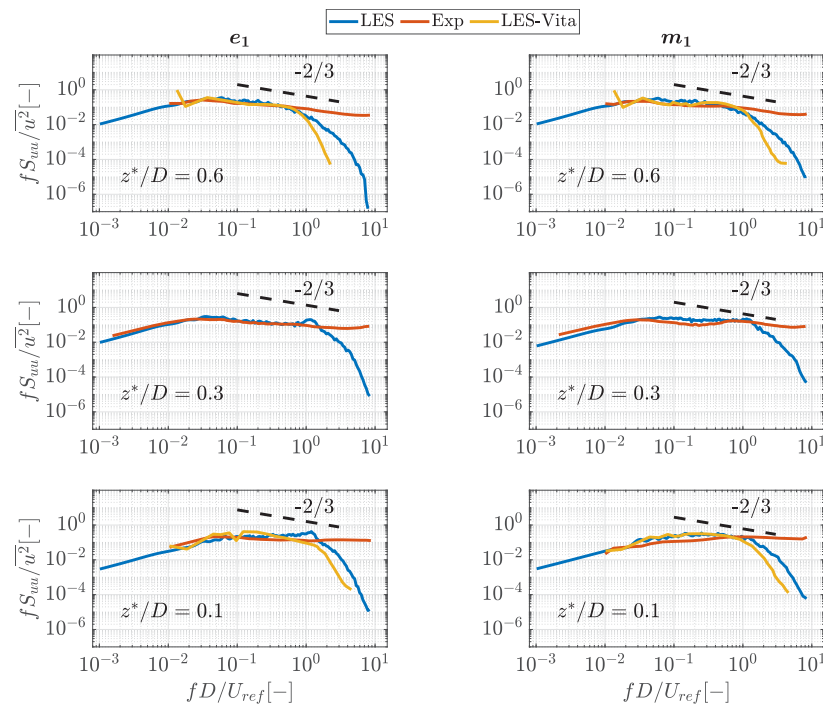


Fig. 11. Normalized spectrum for the u -velocity component, fS_{uu}/\bar{u}^2 , at the rooftop locations e_1 and m_1 and at a non-dimensional height $z^*/D = 0.1, 0.3, 0.6$, with the $-2/3$ slope line. In the figure, the results from the present LES analysis are represented as well as the results from the experimental data and LES-Vita. Note that the normalized spectrum from the experimental data and the LES-Vita are smoothed.

the region closer to the surface, LES results for the e_1 and m_1 locations show an agreement with the LES-Vranešević simulation.

The longitudinal integral length scale in the x -direction, L_x^x , normalized by the building width D is shown in Fig. 10, along the non-dimensional height z^*/D , at various locations over the roof. The strong spatial variation of the integral length scales values, evidenced by the experiment, is well captured by the LES.

In Fig. 11, the normalized spectrum for the u -velocity component, fS_{uu}/\bar{u}^2 , against the non-dimensional frequency fD/U_{ref} , is shown at the locations e_1 and m_1 , and at $z^*/D = 0.1, 0.3, 0.6$. Note that the minimum frequency of the estimated spectra from the simulated LES case $f_{min} = 1/64$ Hz (equivalent to the non-dimensional frequency $fD/U_{ref} = 1.3 \times 10^{-4}$), however, the normalized spectra in Fig. 11 are shown starting from the non-dimensional frequency $fD/U_{ref} = 10^{-3}$. This is done to improve the visualization of the normalized spectra within the frequency region of the available normalized spectra of the reference experiment and LES simulation. It is worth mentioning that the spectra in Fig. 11 are computed using Blackman and Tukey spectrum estimator (Marple, 2019). The normalized spectra acquired from the LES are consistence with the experimental results and LES-Vita. The normalized spectra from the LES simulation exhibit a sharp decline at $fD/U_{ref} > 1$, due to the LES grid cut-off. The fS_{uu}/\bar{u}^2 shows a shift in its peak to high frequencies closer to the surface of the building, which was also observed in the field measurements done by Rotach (1991). A more comprehensive analysis discussing this shift is done in the subsequent Section 6.1.

6. Influence of the high-rise building on the wind field statistical characteristics

In this section, different statistics of the wind velocity field along vertical lines located at positions e_1 and m_1 are compared for Case I (empty domain) and Case II (HRB in the domain). Additionally, statistical characteristics were analyzed at vertical planes perpendicular to the mean wind direction centered at e_1 and m_1 (e_1 -plane and m_1 -plane).

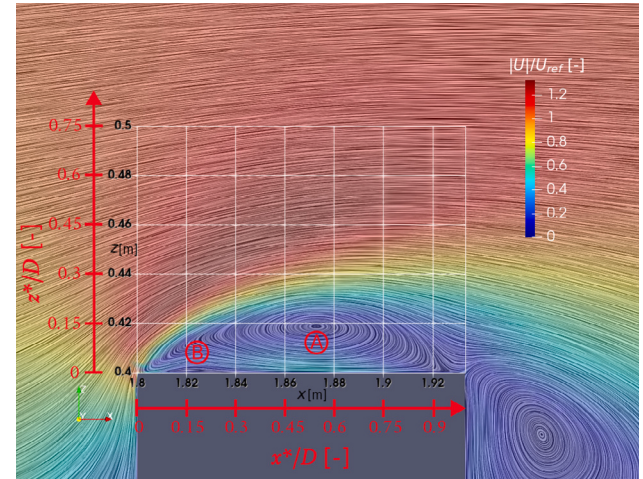


Fig. 12. Modulus of the non-dimensional mean longitudinal velocity component distribution, $|U|/U_{ref}$, with the streamlines in the middle plane of the roof. The points A and B indicate the cross-sections of the recirculation regions over the rooftop.

Also, a vertical plane parallel the mean wind direction centered at m_1 was considered (p -plane).

In Fig. 12, the modulus of the non-dimensional mean longitudinal velocity component distribution, $|U|/U_{ref}$, is depicted with the mean streamlines corresponding to $[U, W]$ vector on the p -plane of the roof. As shown, recirculation patterns are resolved in the mean velocity field over the rooftop. The center of the primary recirculation pattern (point A) is located at $(x^*, z^*) \sim (0.56D, 0.11D)$ m from the windward edge and the HRB rooftop. The maximum thickness of the primary recirculation bubble is $\sim 0.23D$ m from the roof surface. A thin recirculation pattern (point B) was observed at $x^* \sim 0.15D$ m close to the windward edge, which was also noticed in the LES simulation done by Vranešević et al. (2022).

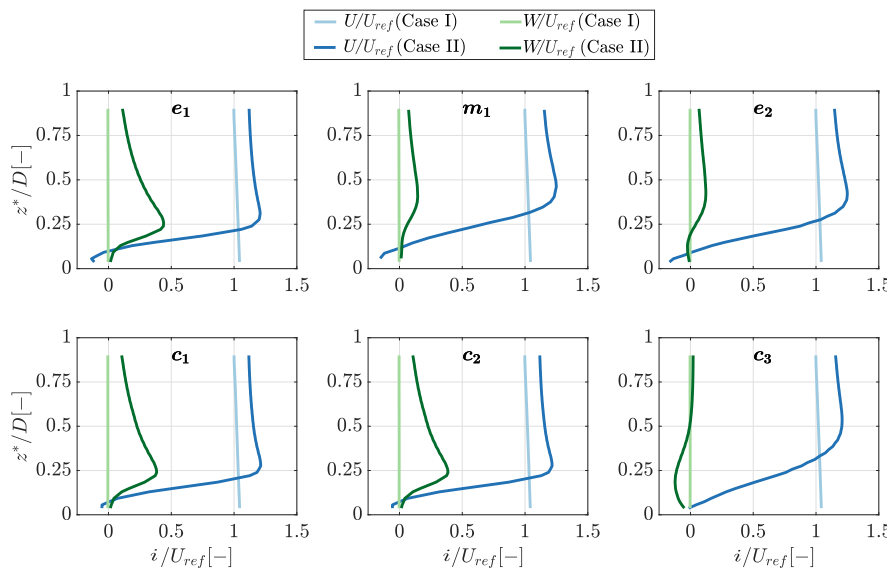


Fig. 13. Vertical profiles of the non-dimensional mean wind velocity components, i/U_{ref} (for $i = U, W$), evaluated from the LES, at the rooftop locations shown in Fig. 1(b), for Case I (empty domain) and Case II (HRB in the domain).

6.1. Wind velocity characteristics along vertical lines

The vertical profiles of the mean velocity components U and W are shown in Fig. 13. The results show the well known variation of the velocity component U over the building, with respect to its values in the unperturbed case I. This is a relative decrease in velocity near the rooftop and an increase in higher positions, which is compatible with the existence of the recirculation bubble. This pattern of the wind velocity above the building has been documented several times. For instance, it was also observed in the RANS simulations of the wind flow over a flat rooftop done by Abohela et al. (2013) and Toja-Silva et al. (2015). The vertical profiles of the W over the rooftop (Case II), also exhibit the expected variations relative to the undisturbed values (Case I), hence significantly positive and negative values in the windward side, respectively, which is an evidence of the expected detachment bubble pattern.

The turbulence intensity for the three velocity components I_u , I_v and I_w , is shown in Fig. 14. For Case I, the absence of the building leads to nearly constant values of the turbulence intensities for the three velocity components $I_i \sim 13\%$. In presences of the HRB, the three turbulence intensities exhibit high values close to the rooftop surface. Far from the rooftop, the turbulence intensities are nearly constant and similar to the undisturbed value at all the rooftop locations. It is important to note that the Normal Turbulence Model (NTM) used in the IEC 61400-2 Standards provides lower turbulence intensities in the region close to the surface, particularly inside the recirculation bubble, for the same wind speed range compared to the actual turbulence intensities observed. This discrepancy needs to be considered during the design process of urban SWTs, as higher turbulence intensities near the rooftop could significantly impact the fatigue loading behavior of SWTs operating on buildings.

The non-dimensional longitudinal integral length scale for the three wind velocity components, L_i^x/D , for $i = u, v, w$, are shown in Fig. 15. In the absence of the building, the L_i^x/D exhibits low variation with height for the three velocity components. L_v^x/D and L_w^x/D have nearly the same value ~ 1.2 , and L_u^x/D is ~ 2.7 for all rooftop locations. Whilst the HRB introduces a strong spatial dependence with the distance to the rooftop for the L_i^x/D .

The normalized PSD for the u , v and w -velocity components, $f S_{ii}/i^2$, at non-dimensional heights $z^*/D = 0.1, 0.3, 0.6$, is shown in Fig. 16 (at location m_1) against the non-dimensional frequency $f D/U_{ref}$ together with $-2/3$ slope. The peak frequency, which is the frequency that

corresponds to the highest value of the normalized spectra, depends on the distance to the surface of the rooftop for Case II. The peak frequency of normalized spectra exhibits a shift to high frequencies as the distance to the building rooftop decreases. In order to further analyze the mentioned frequency shift, the normalized spectra are plotted in Fig. 17 (at location m_1) as colormap plots dependent on the non-dimensional z^*/D and non-dimensional frequency $f D/U_{ref}$. For Case I, the peak frequency shows no dependence on height. Whilst, for Case II, a shift in the peak frequency is observed as the rooftop is approached. This type of shifts in the peak frequency needs to be well represented in the two-points two-times second-order statistics of the wind field provided as inputs to the numerical generation methods during the synthesis process of the wind velocity fields, since the shapes of spectra and cross-spectra are directly related to the fatigue loading of wind turbines.

The coherence function is evaluated for two non-dimensional vertical separation distances $\Delta z/D = 3.6 - 3.3 = 0.3$ (where $\Delta z = z_2 - z_1$) and $\Delta z/D = 3.6 - 3.1 = 0.5$. In Fig. 18, the coherence function is shown against the $f D/U_{ref}$. In general, the coherence functions for all cases exhibit the expected decay when the normalized frequency increases. This decay presents an asymptote at a value of 0.15 and not towards 0, this could be due to the fact that the coherence function defined in Eq. (2) is a biased estimator (Kristensen and Kirkegaard, 1986) and/or associated with the numerical noise as reported in the study done by Shaler et al. (2019). Additionally, as expected, increasing the vertical separation leads to a faster decay in the coherence function for both Case I and II. The decay rate for the coherence function of the u -velocity component is faster compared to the v and w -velocity components at the two rooftop locations analyzed. It was noticed that the decay rate for Case I is generally lower than for Case II at both e_1 and m_1 locations. The lower decay rate in Case I shows that the turbulent wind field is more coherent over larger distances compared to Case II. Moreover, the decay rate of the coherence functions at location e_1 was observed to be lower compared to the decay rate at the m_1 location, which is coherent with the fact that location m_1 is deep immersed in the recirculation region where coherence is rapidly lost.

The normalized ACF, $\gamma_{ii}(\tau)/\gamma_{ii}(0)$ (for $i = u, v, w$), is shown against the time lag, $\tau (= t_2 - t_1)$, and the non-dimensional height z^*/D in Fig. 19 for location m_1 . It is worth mentioning that the ACF was calculated by using the biased ACF estimator as recommended in Marple (2019). For Case I, the decay rate of the ACF is constant with the non-dimensional height z^*/D for the three velocity components and the decay rate of

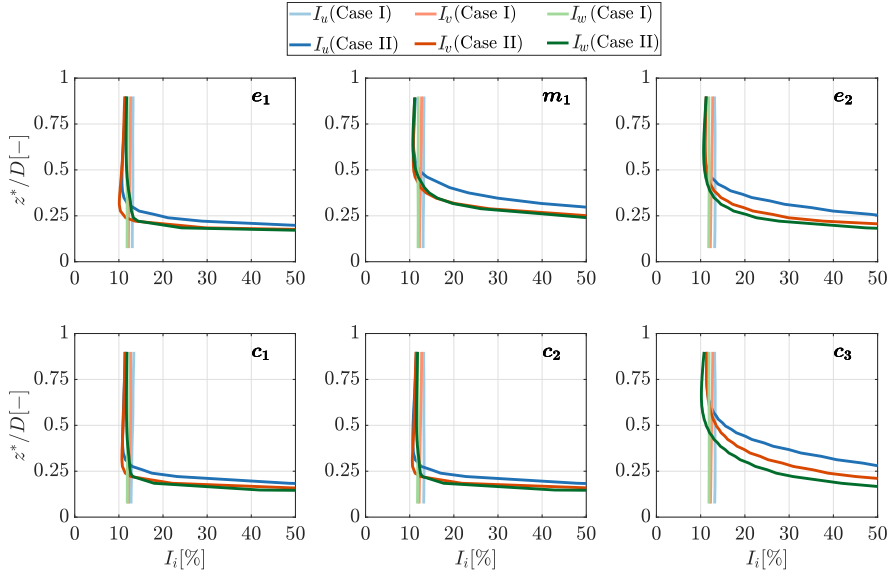


Fig. 14. Vertical profiles of the turbulence intensities, I_i , for $i = u, v, w$, evaluated from the LES, at the rooftop locations shown in Fig. 1(b), for Case I (empty domain) and Case II (HRB in the domain).

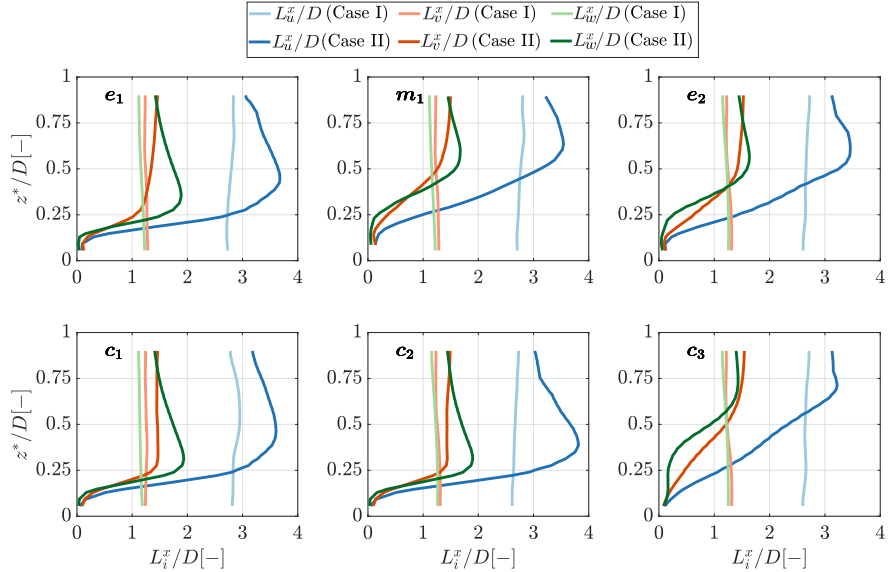


Fig. 15. Vertical profiles of the non-dimensional longitudinal integral length scales, L_i^x/D for $i = u, v, w$, evaluated from the LES, at the rooftop locations shown in Fig. 1(b), for Case I (empty domain) and Case II (HRB in the domain).

the ACF of the u -velocity components is slower than for the v and w -velocity components. Whilst for Case II, the decay rate depends on the distance to the rooftop, since it decays faster in the vicinity of the rooftop. A damped sinusoidal oscillation in the normalized ACF for the vertical velocity was observed inside the recirculation region at m_1 location. The faster decay in the ACF closer to the surface reflects the influence of the building on the second-order statistics. Properly considering these characteristics into the second-order statistics is crucial for the numerical generation of realistic synthetic wind velocity fields to be used in aeroelastic simulations. Integrating these realistic second order statistical characteristics with the numerical generation methods of synthetic velocity fields ensures a more precise representation of the loads acting on urban SWTs.

6.2. Analysis of wind flow characteristics on span-wise vertical planes

The statistics of the wind velocity field have been resolved on two vertical planes. The two of them are perpendicular to the mean wind

direction over the HRB. The two perpendicular planes are located at $x^* = 0.2D$ (centered at the windward point e_1) and $x^* = 0.5D$ (centered at the middle point m_1), where $x^* = x - 4.5H$. Note that the perpendicular planes will be referred to as the e_1 -plane and m_1 -plane, respectively, in the rest of this section.

The normalized mean wind velocity components is shown in Fig. 20 on the e_1 -plane and m_1 -plane. The thickness of the recirculation region depends on the longitudinal direction as it changes from e_1 -plane to m_1 -plane.

The spatial distribution of longitudinal integral length scales of the three velocity components on e_1 -plane and m_1 -plane is shown in Fig. 21. For both planes, the integral length scales distribution presents the expected lateral symmetry. Both the L_v^x and L_w^x converge to almost similar constant values at $z^*/D > 0.7$.

Similarly as for the integral length scales, the non-dimensional standard deviation for the wind velocity components, σ_i/U_{ref} , shows a level of homogeneity in the y -direction at all height levels ($z^*/D > 0.3$

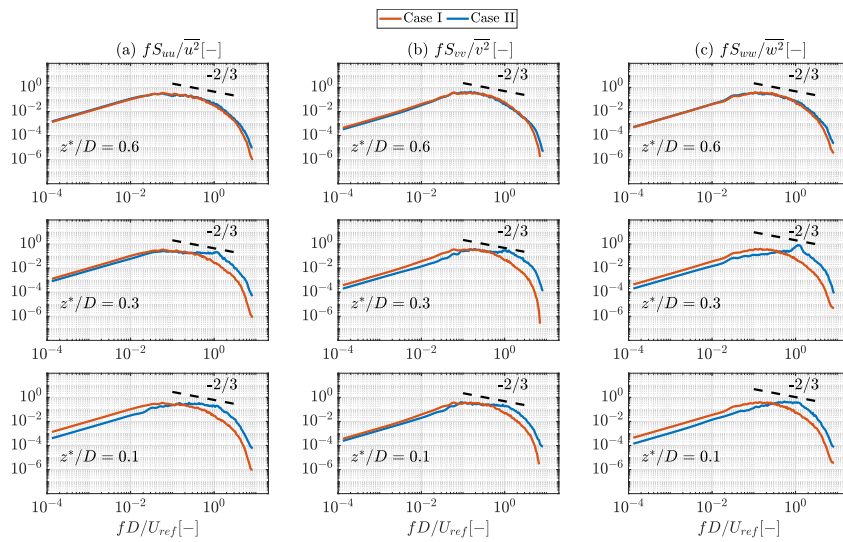


Fig. 16. Normalized PSD, fS_{ii}/\bar{i}^2 for $i = u, v, w$, against the non-dimensional frequency, fD/U_{ref} , at the rooftop locations m_1 and at a non-dimensional height $z^*/D = 0.1, 0.3, 0.6$, evaluated from the LES simulation, for Case I and Case II.

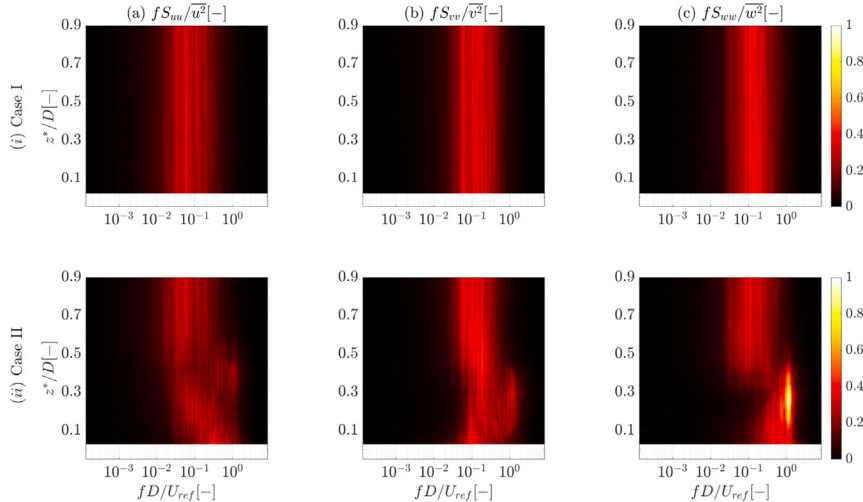


Fig. 17. Normalized PSD, fS_{ii}/\bar{i}^2 , for $i = (a) u$, (b) v , and (c) w , velocity components, against the non-dimensional frequency, fD/U_{ref} , and the non-dimensional vertical direction, z^*/D , for Case I and Case II at the rooftop location m_1 .

and 0.4, for e_1 and m_1 planes, respectively), as depicted in Fig. 22. Moreover, the σ_i/U_{ref} values for the three velocity components tend to a constant value at the homogeneous regions, which indicates the isotropy of the wind characteristics in these regions as well.

7. Conclusions

In the presented work, Large Eddy Simulation (LES) was employed to replicate a reference experimental study and references LES studies for a High-Rise Building (HRB). This study aims to gain a deeper understanding of the statistical characteristics of the wind field over a HRB with a turbulent inflow characterized by Eurocode Terrain Type II. This study commonly examined statistics such as means, variances, length scales, spectra, and cross-spectra. In addition, this study investigates less commonly explored statistics, including two-points two-times second order statistics, which are essential inputs for numerical generation methods of wind fields. Accurately representing these statistics is crucial for generating synthetic urban wind fields that replicate real conditions. This, in turn, leads to better predictions of power performance and urban wind loads on wind turbines during the aeroelastic design process.

The turbulent inflow was generated using the spectral representation method, particularly using Mann's approach for the synthetic generation of the turbulent wind field. A parametric study was conducted to identify the value of the parameters necessary for the synthetic generation of the wind field to acquire the desired turbulent inflow observed in the experimental study. Some discrepancies in the statistical values characterizing the turbulent inflow have been observed. Achieving a better match for inflow turbulence descriptors, such as the vertical profiles of longitudinal intensity, is crucial, as these inflow characteristics, among others, significantly influence the size of the recirculation bubble formed on top of the HRB.

The significant influence of the HRB on the surrounding flow has been quantified through modifications in the mean velocity field, turbulence intensities, spectra, and cross-spectra at specific points. These modifications reveal clear differences when compared to the undisturbed inflow at the same locations, as well as to the spectral forms presented in current wind turbine design standards. The longitudinal mean wind velocity exhibits acceleration outside the boundary layer and the height of the maximum longitudinal mean wind velocity is dependent on the boundary layer thickness. In the proximity to the building's surface, elevated levels of turbulence intensities were

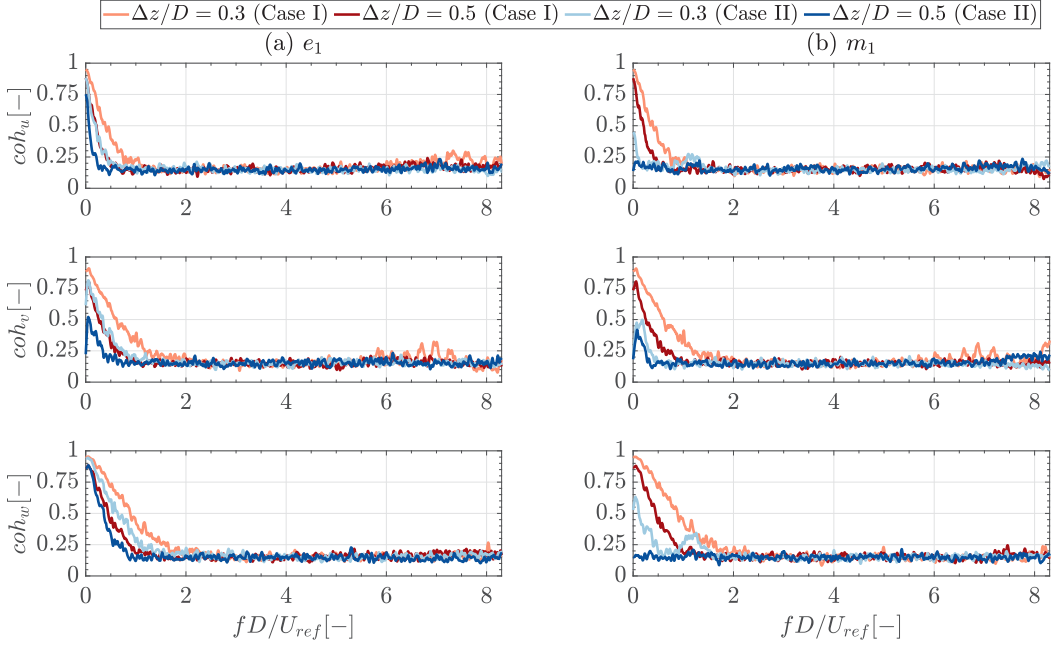


Fig. 18. Coherence, coh_i for $i = u, v, w$, in terms of the non-dimensional frequency fD/U_{ref} , for non-dimensional vertical separation, $\Delta z/D = 0.3$ and 0.5, at the rooftop location e_1 , evaluated from the LES simulation, for Case I and Case II.

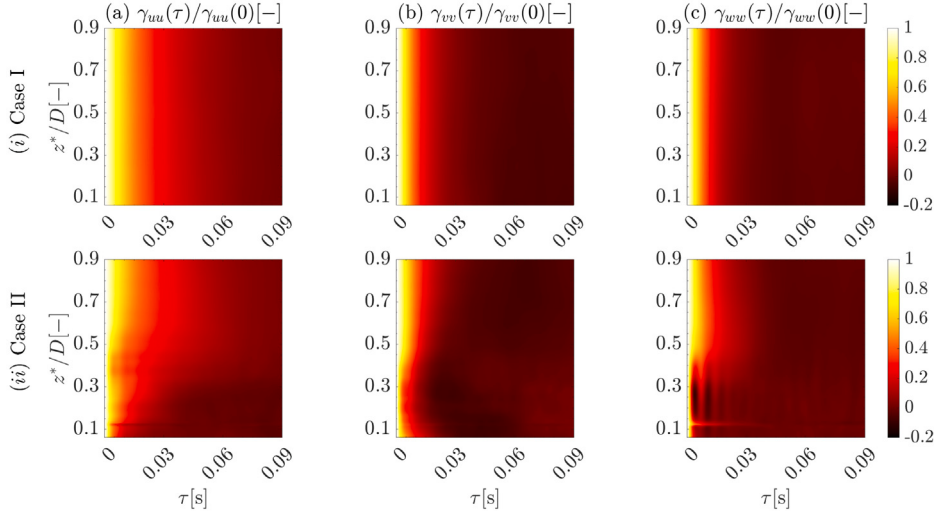


Fig. 19. Normalized ACF, $\gamma_{ij}(\tau)/\gamma_{ij}(0)$, for $i =$ (a) u , (b) v , and (c) w , velocity components, against the time lag, τ , and the non-dimensional vertical direction, z^*/D , for Case I and Case II at the rooftop location m_1 .

acquired and they are dependent on the boundary layer thickness. Moreover, the high levels of turbulence intensities decrease as the distance from the surface increases. In general, the spectra and its Fourier pair (the autocovariance function), exhibit similar characteristics for the two considered cases in the region far away from the building surface, although, a noticeable difference arises in the region close to the building surface. A shift in the peak of the normalized spectra to high frequencies was observed closer to the building surface. The temporal autocovariance function exhibits faster decay in the region inside the boundary layer compared to the region outside the boundary layer.

The two-points two-times second-order statistics of wind velocity components resolved from the present LES are significantly impacted by the presence of the building. This effect is particularly evident in the spatial coherence function of the three velocity components at two different vertical positions. The building causes a more pronounced

decrease in coherence functions as the normalized frequency increases, compared to the empty case. Additionally, in the middle of the recirculation patterns, distinct peaks in the coherence function at specific values of the normalized frequency are observed for all three velocity components, indicating a clear periodic signature. These alterations in second-order statistics, induced by the building, are likely to strongly influence the dynamic loading of wind turbines operating in such environments. Therefore, these effects must be considered when generating synthetic wind velocity fields for use in aeroelastic simulations of wind turbines.

Finally, the two-points two-times second-order statistics resolved from the performed LES exhibit promising quality to serve as deterministic input for the numerical generation methods for synthetic wind fields in highly non-homogeneous conditions, such as those over complex terrains, urban environments, or wind turbine wakes.

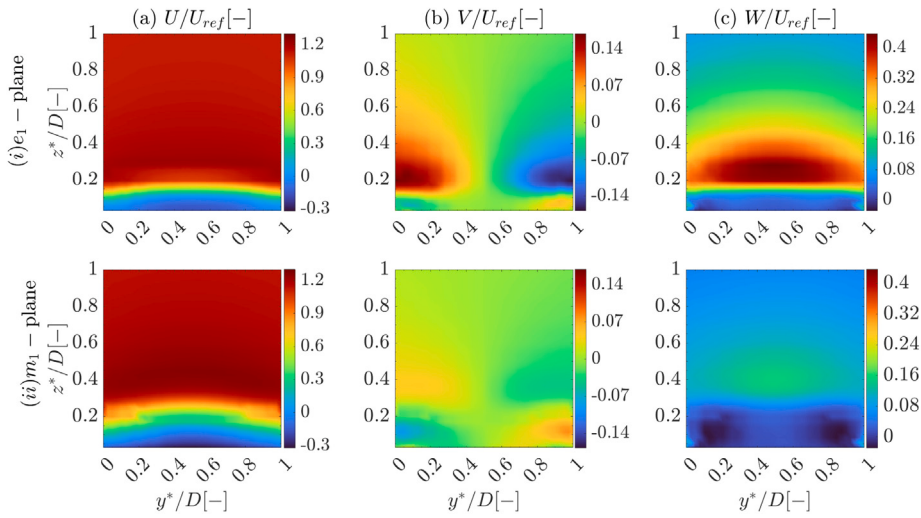


Fig. 20. Normalized mean velocity distribution for the (a) longitudinal, $U/U_{ref}[-]$, (b) lateral, $V/U_{ref}[-]$, and (c) vertical, $W/U_{ref}[-]$, velocity components, against the non-dimensional lateral direction, y^*/D , and the non-dimensional vertical direction, z^*/D , for Case II (i) e_1 -plane and (ii) m_1 -plane.

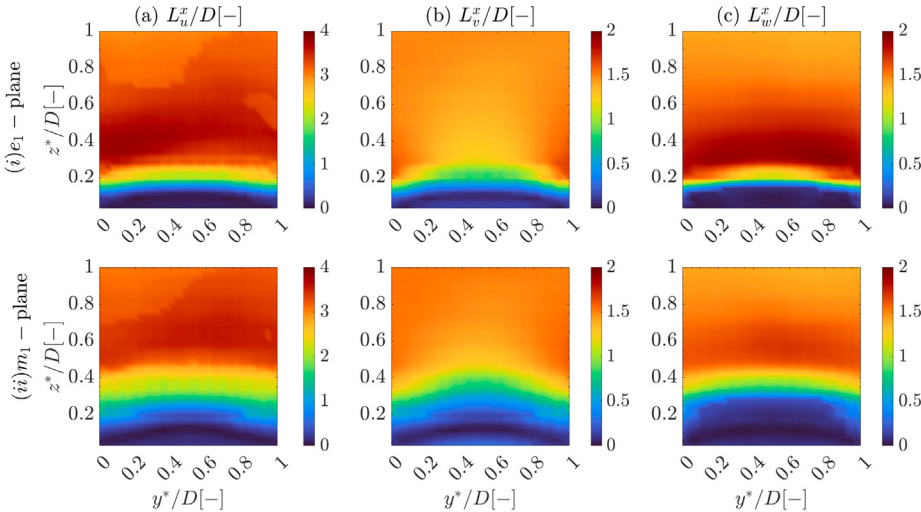


Fig. 21. Normalized longitudinal integral length scales distribution for the (a) longitudinal, $L_u^x/D[-]$, (b) lateral, $L_v^x/D[-]$, and (c) vertical, $L_w^x/D[-]$, velocity components, against the non-dimensional lateral direction, y^*/D , and the non-dimensional vertical direction, z^*/D , for Case II (i) e_1 -plane and (ii) m_1 -plane.

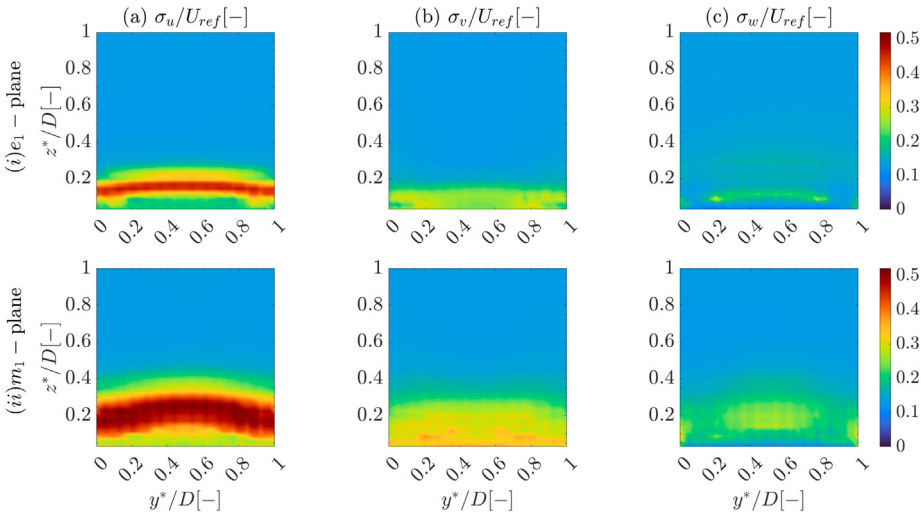


Fig. 22. Non-dimensional standard deviation distribution for the (a) longitudinal, $\sigma_u/U_{ref}[-]$, (b) lateral, $\sigma_v/U_{ref}[-]$, and (c) vertical, $\sigma_w/U_{ref}[-]$, velocity components, against the non-dimensional lateral direction, y^*/D , and the non-dimensional vertical direction, z^*/D , for Case II (i) e_1 -plane and (ii) m_1 -plane.

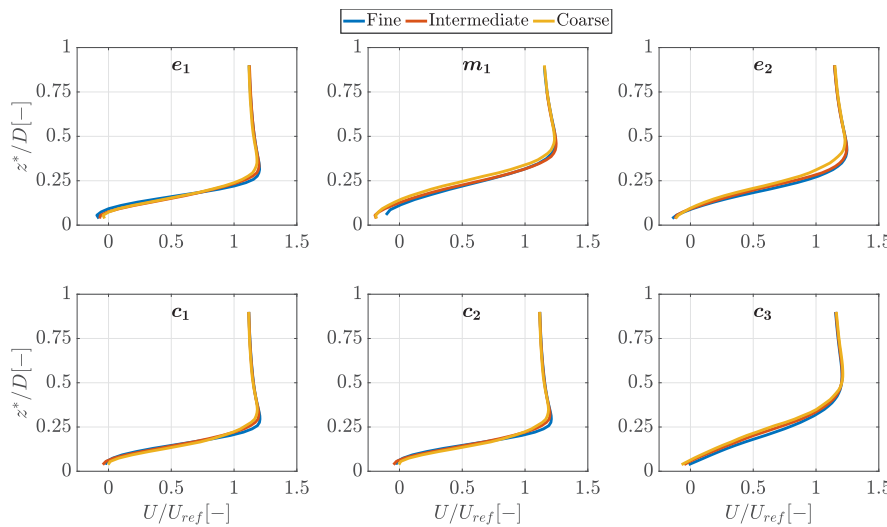


Fig. 23. Non-dimensional mean longitudinal velocity component, U/U_{ref} , against the non-dimensional height, z^*/D , for coarse, intermediate and fine mesh grid (see Table 1), at different vertical lines over the rooftop locations shown in Fig. 1(b).

CRediT authorship contribution statement

Mohanad Elagamy: Writing – original draft, Validation, Software, Methodology, Investigation, Data curation, Conceptualization. **Nishchay Tiwari:** Writing – original draft, Software, Conceptualization. **Cristobal Gallego-Castillo:** Writing – review & editing, Supervision, Methodology. **Alvaro Cuerva-Tejero:** Writing – review & editing, Supervision, Methodology. **Oscar Lopez-Garcia:** Writing – review & editing, Supervision. **Sergio Avila-Sanchez:** Writing – review & editing, Supervision.

Declaration of competing interest

The authors declare that they have no known competing financial interests or personal relationships that could have appeared to influence the work reported in this paper.

Acknowledgments

This research has been undertaken as a part of the zEPHYR project. This project has received funding from the European Union's Horizon 2020 research and innovation programme under Grant Agreement No EC grant 860101. The authors would like to acknowledge CESVIMA for their support in providing computer resources for this research. Also, the authors would like to express their sincere appreciation to the Department of Aircraft and Aerospace Vehicles of UPM for their generous provision of computers and space for this research.

Appendix

In Fig. 23, the non-dimensional longitudinal velocity profile, U/U_{ref} , for coarse, intermediate, and fine were compared for the grid independency study. It was observed that the “fine” mesh is sufficiently refined and the discrepancy between the intermediate and the fine mesh is negligible. The velocity components are compared at six different locations and the trend is consistent. The difference between the maximum U_{max}/U_{ref} in the fine and the intermediate grids is 0.38% and 0.3% for locations e_1 and m_1 , respectively. Whilst, the difference between the U_{max}/U_{ref} in the fine and the coarse grids is 1.92% and 1.36% for locations e_1 and m_1 , respectively.

Data availability

Data will be made available on request.

References

- Abohela, I., Hamza, N., Dudek, S., 2013. Effect of roof shape, wind direction, building height and urban configuration on the energy yield and positioning of roof mounted wind turbines. Renew. Energy 50, 1106–1118. <http://dx.doi.org/10.1016/j.renene.2012.08.068>, Retrieved from <https://www.sciencedirect.com/science/article/pii/S0960148112005381>.
- AIJ, 2007. Architectural institute of Japan, guidebook for CFD predictions of urban wind environment. Retrieved from https://www.aij.or.jp/jpn/publish/cfdguide/index_e.htm.
- Blocken, B., 2015. Computational Fluid Dynamics for urban physics: Importance, scales, possibilities, limitations and ten tips and tricks towards accurate and reliable simulations. Build. Environ. 91, 219–245. <http://dx.doi.org/10.1016/j.buildenv.2015.02.015>, Retrieved from <https://www.sciencedirect.com/science/article/pii/S0360132315000724>.
- Blocken, B., 2018. LES over RANS in building simulation for outdoor and indoor applications: A foregone conclusion? Build. Simul. 11 (4), 821–870. <http://dx.doi.org/10.1007/s12273-018-0459-3>.
- Brook, R., 1972. The measurement of turbulence in a city environment. J. Appl. Meteorol. Climatol. 11 (3), 443–450. [http://dx.doi.org/10.1175/1520-0450\(1972\)011\textless443\textgreater0443:TMOTIA\textless450](http://dx.doi.org/10.1175/1520-0450(1972)011\textless443\textgreater0443:TMOTIA\textless450).
- Burton, T., Jenkins, N., Sharpe, D., Bossanyi, E., 2011. Wind Energy Handbook. John Wiley & Sons, Ltd, <http://dx.doi.org/10.1002/9781119992714>.
- CEDVAL, 2006. Compilation of Experimental Data for Validation of Microscale Dispersion Models. Hamburg University, Hamburg, Germany.
- Christen, A., van Gorsel, E., Vogt, R., 2007. Coherent structures in urban roughness sublayer turbulence. Int. J. Climatol. 27 (14), 1955–1968. <http://dx.doi.org/10.1002/joc.1625>, Retrieved from <https://rmets.onlinelibrary.wiley.com/doi/abs/10.1002/joc.1625>.
- Dimitrov, N., Natarajan, A., Mann, J., 2017. Effects of normal and extreme turbulence spectral parameters on wind turbine loads. Renew. Energy 101, 1180–1193. <http://dx.doi.org/10.1016/j.renene.2016.10.001>, Retrieved from <https://www.sciencedirect.com/science/article/pii/S0960148116308655>.
- Elagamy, M., Gallego-Castillo, C., Cuerva-Tejero, A., Lopez-Garcia, O., Avila-Sanchez, S., 2023. Eigenanalysis of vector autoregressive model for optimal fitting of a predefined cross power spectral density matrix: Application to numeric generation of stationary homogeneous isotropic/anisotropic turbulent wind fields. J. Wind Eng. Ind. Aerodyn. 238, 105420. <http://dx.doi.org/10.1016/j.jweia.2023.105420>, Retrieved from <https://www.sciencedirect.com/science/article/pii/S016761052300123X>.
- Eliasson, I., Offerle, B., Grimmond, C., Lindqvist, S., 2006. Wind fields and turbulence statistics in an urban street canyon. Atmos. Environ. 40 (1), 1–16. <http://dx.doi.org/10.1016/j.atmosenv.2005.03.031>, Retrieved from <https://www.sciencedirect.com/science/article/pii/S1352231005002967>.

- Emes, M., Arjomandi, M., Kelso, R., Ghanadi, F., 2016. Integral length scales in a low-roughness atmospheric boundary layer. In: Proceedings of the 18th Australasian Wind Engineering Society Workshop. Australasian Wind Engineering Society, McLaren Vale, South Australia, pp. 1–4, Retrieved from <https://hdl.handle.net/2440/109454>.
- Eurocode, 2005. Eurocode 1: Actions on Structures - Part 1-4: General Actions - Wind Actions. Technical Report EN 1991-1-4, CEN, Brussels, Belgium.
- Feigenwinter, C., Vogt, R., Parlow, E., 1999. Vertical structure of selected turbulence characteristics above an urban canopy. *Theor. Appl. Climatol.* 62 (1), 51–63. <http://dx.doi.org/10.1007/s007040050074>.
- Fortuniak, K., Pawlik, W., 2015. Selected spectral characteristics of turbulence over an urbanized area in the centre of Łódź, Poland. *Bound.-Layer Meteorol.* 154 (1), 137–156. <http://dx.doi.org/10.1007/s10546-014-9966-7>.
- Franke, J., Hellsten, A., Schlünzen, H., Carissimo, B., 2007. Best Practice Guideline for the CFD Simulation of Flows in the Urban Environment: COST Action 732 Quality Assurance and Improvement of Microscale Meteorological Models. Meteorological Institute.
- Gallego-Castillo, C., Cuerva-Tejero, A., Elagamy, M., Lopez-Garcia, O., Avila-Sanchez, S., 2021. A tutorial on reproducing a predefined autocovariance function through AR models: application to stationary homogeneous isotropic turbulence. *Stoch. Environ. Res. Risk Assess.* 36, 1–26. <http://dx.doi.org/10.1007/s00477-021-02156-0>.
- Guo, F., Mann, J., 2022. MannTurb4D_v1 (version v1.0). <http://dx.doi.org/10.5281/zenodo.6223785>, Zenodo. Initial release of the 4D Mann Turbulence Generator.
- Hemida, H., Šarkić, A., 2014. Final Report of a Short Term Scientific Mission COST Action TU1304: Wind Tunnel Tests–Air Flow Around Buildings. Technical Report, WINERCOST, Retrieved from http://winercost.com/cost_files/STSM_report-Sarkic_Hemida.pdf.
- Hemida, H., Šarkić-Glumac, A., Vita, G., Kostadinović Vranešević, K., Höffer, R., 2020. On the flow over high-rise building for wind energy harvesting: an experimental investigation of wind speed and surface pressure. *Appl. Sci.* 10 (15), <http://dx.doi.org/10.3390/app10155283>.
- IEC 61400-2, 2019. Wind Turbines Part 2: Design Requirements for Small Wind Turbines-Annex M, 3 ed. International Electrotechnical Commission.
- Issa, R., 1986. Solution of the implicitly discretized fluid flow equations by operator-splitting. *J. Comput. Phys.* 62 (1), 40–65. [http://dx.doi.org/10.1016/0021-9991\(86\)90099-9](http://dx.doi.org/10.1016/0021-9991(86)90099-9).
- Jacob, J., Sagaut, P., 2018. Wind comfort assessment by means of large eddy simulation with lattice Boltzmann method in full scale city area. *Build. Environ.* 139, 110–124. <http://dx.doi.org/10.1016/j.buildenv.2018.05.015>, Retrieved from <https://www.sciencedirect.com/science/article/pii/S0360132318302750>.
- Kaimal, J.C., Finnigan, J.J., 1994. Atmospheric Boundary Layer Flows: Their Structure and Measurement. Oxford University Press.
- Kaimal, J.C., Wyngaard, J., Izumi, Y., Coté, O., 1972. Spectral characteristics of surface-layer turbulence. *Q. J. R. Meteorol. Soc.* 98 (417), 563–589.
- KC, A., Whale, J., Urmee, T., 2019. Urban wind conditions and small wind turbines in the built environment: A review. *Renew. Energy* 131, 268–283. <http://dx.doi.org/10.1016/j.renene.2018.07.050>, Retrieved from <https://www.sciencedirect.com/science/article/pii/S0960148118308474>.
- Kono, T., Kogaki, T., Kiwata, T., 2016. Numerical investigation of wind conditions for roof-mounted wind turbines: effects of wind direction and horizontal aspect ratio of a high-rise cuboid building. *Energies* 9 (11), 907. <http://dx.doi.org/10.3390/en9110907>.
- Krenk, S., Møller, R., 2019. Turbulent wind field representation and conditional mean-field simulation. *Proc. R. Soc. A* 475 (2223), 20180887. <http://dx.doi.org/10.1098/rspa.2018.0887>.
- Kristensen, L., Kirkegaard, P., 1986. Sampling Problems with Spectral Coherence. In: Denmark. Forskningscenter Risoe. Risoe-R, (526), Risø National Laboratory, Retrieved from <https://orbit.dtu.dk/en/publications/sampling-problems-with-spectral-coherence>.
- Lilly, D.K., 1962. On the numerical simulation of buoyant convection. *Tellus* 14 (2), 148–172. <http://dx.doi.org/10.3402/tellusa.v14i2.9537>.
- Mann, J., 1994. The spatial structure of neutral atmospheric surface-layer turbulence. *J. Fluid Mech.* 273, 141–168. <http://dx.doi.org/10.1017/S0022112094001886>.
- Mann, J., 1998. Wind field simulation. *Probab. Eng. Mech.* 13 (4), 269–282. [http://dx.doi.org/10.1016/S0266-8920\(97\)00036-2](http://dx.doi.org/10.1016/S0266-8920(97)00036-2).
- Marple, Jr., S.L., 2019. Digital Spectral Analysis, second ed. Dover Publications, New York, Retrieved from <https://www.doverpublications.com/048678052x/>.
- Merlier, L., Jacob, J., Sagaut, P., 2019. Lattice-Boltzmann large-eddy simulation of pollutant dispersion in complex urban environment with dense gas effect: Model evaluation and flow analysis. *Build. Environ.* 148, 634–652. <http://dx.doi.org/10.1016/j.buildenv.2018.11.009>, Retrieved from <https://www.sciencedirect.com/science/article/pii/S0360132318307042>.
- Micallef, D., Van Bussel, G., 2018. A review of urban wind energy research: aerodynamics and other challenges. *Energies* 11 (9), <http://dx.doi.org/10.3390/en11092204>, Retrieved from <https://www.mdpi.com/1996-1073/11/9/2204>.
- Musial, W., Ram, B., 2010. Large-scale Offshore Wind Power in the United States: Assessment of Opportunities and Barriers. Technical Report NREL/TP-500-40745, National Renewable Energy Lab.(NREL), Golden, CO (United States), <http://dx.doi.org/10.2172/990101>, Retrieved from <https://www.nrel.gov/docs/fy10osti/40745.pdf>.
- Nelson, M.A., Brown, M.J., Pardyjak, E.R., Klewicki, J.C., 2004. Turbulence within and above real and artificial urban canopies. In: AMS 5th Symposium on the Urban Environment. Retrieved from <https://www.osti.gov/biblio/977786>.
- Nelson, M.A., Pardyjak, E.R., Brown, M.J., Klewicki, J.C., 2007a. Properties of the wind field within the Oklahoma City Park Avenue street canyon. Part II: Spectra, spectra, and quadrant analyses. *J. Appl. Meteorol. Climatol.* 46 (12), 2055–2073. <http://dx.doi.org/10.1175/2006JAMC1290.1>.
- Nelson, M.A., Pardyjak, E.R., Klewicki, J.C., Pol, S.U., Brown, M.J., 2007b. Properties of the wind field within the Oklahoma City Park Avenue street canyon. Part I: Mean flow and turbulence statistics. *J. Appl. Meteorol. Climatol.* 46 (12), 2038–2054. <http://dx.doi.org/10.1175/2006JAMC1427.1>, Retrieved from <https://journals.ametsoc.org/view/journals/apme/46/12/2006jmc1427.1.xml>.
- Nicoud, F., Ducros, F., 1999. Subgrid-scale stress modelling based on the square of the velocity gradient tensor. *Flow Turbul. Combust.* 62 (3), 183–200. <http://dx.doi.org/10.1023/A:100995426001>.
- Panofsky, H.A., Dutton, J.A., 1984. Atmospheric Turbulence. John Wiley & Sons, New York.
- Patankar, S., Spalding, D., 1972. A calculation procedure for heat, mass and momentum transfer in three-dimensional parabolic flows. *Int. J. Heat Mass Transfer* 15 (10), 1787–1806. [http://dx.doi.org/10.1016/0017-9310\(72\)90054-3](http://dx.doi.org/10.1016/0017-9310(72)90054-3).
- Peng, H., Dai, S., Lin, K., Hu, G., Liu, H., 2020. Experimental investigation of wind characteristics and wind energy potential over rooftops: Effects of building parameters. *J. Wind Eng. Ind. Aerodyn.* 205, 104304. <http://dx.doi.org/10.1016/j.jweia.2020.104304>.
- Pope, S.B., 2000. Turbulent Flows. Cambridge University Press, <http://dx.doi.org/10.1017/CBO9780511840531>.
- Ricciardelli, F., Polimeno, S., 2006. Some characteristics of the wind flow in the lower Urban Boundary Layer. *J. Wind Eng. Ind. Aerodyn.* 94 (11), 815–832. <http://dx.doi.org/10.1016/j.jweia.2006.06.003>, Retrieved from <https://www.sciencedirect.com/science/article/pii/S0167610506000894>.
- Rotach, M., 1991. Turbulence Within and Above an Urban Canopy (Ph.D. thesis). ETH Zurich, <http://dx.doi.org/10.3929/ethz-a-000599740>.
- Roth, M., 2000. Review of atmospheric turbulence over cities. *Q. J. R. Meteorol. Soc.* 126 (564), 941–990. <http://dx.doi.org/10.1002/qj.49712656409>, Retrieved from <https://rmets.onlinelibrary.wiley.com/doi/abs/10.1002/qj.49712656409>.
- Šarkić-Glumac, A., Hemida, H., Höffer, R., 2018a. Wind energy potential above a high-rise building influenced by neighboring buildings: An experimental investigation. *J. Wind Eng. Ind. Aerodyn.* 175, 32–42. <http://dx.doi.org/10.1016/j.jweia.2018.01.022>.
- Šarkić-Glumac, A., Hemida, H., Höffer, R., 2018b. Wind tunnel experimental data for flow characteristics above the roof of high-rise buildings in group arrangement for wind energy harvesting. Mendeley Data, <http://dx.doi.org/10.17632/cxc4w2myyw.2>.
- Šarkić-Glumac, A., Hemida, H., Vita, G., Kostadinović Vranešević, K., Höffer, R., 2020. Wind Tunnel Experimental Data for Flow Characteristics above the Roof of Isolated High-rise Building for Wind Energy Harvesting Considering Two Shapes of the Roof, Flat Roof and Deck Roof. Mendeley Data, <http://dx.doi.org/10.17632/jp7vc8tf7w.1>.
- Shaler, K., Jonkman, J., Doubrava Moreira, P., Hamilton, N., 2019. FAST.Farm response to varying wind inflow techniques. In: AIAA Scitech 2019 Forum. San Diego, California, <http://dx.doi.org/10.2514/6.2019-2086>.
- Smagorinsky, J., 1963. General circulation experiments with the primitive equations. Part I: The basic experiment. *Mon. Weather Rev.* 91, 99–164. [http://dx.doi.org/10.1175/1520-0493\(1963\)091<099:GCEWT>2.3.CO;2](http://dx.doi.org/10.1175/1520-0493(1963)091<099:GCEWT>2.3.CO;2).
- Smith, J., Forsyth, T., Sinclair, K., Oteri, F., 2012. Built-environment Wind Turbine Roadmap. Technical Report, National Renewable Energy Lab.(NREL), Golden, CO (United States), Retrieved from <https://www.nrel.gov/docs/fy13osti/50499.pdf>.
- Stathopoulos, T., Alrawashdeh, H., Al-Quraan, A., Blocken, B., Dilimulati, A., Paraschivoiu, M., Pilay, P., 2018. Urban wind energy: Some views on potential and challenges. *J. Wind Eng. Ind. Aerodyn.* 179, 146–157. <http://dx.doi.org/10.1016/j.jweia.2018.05.018>, Retrieved from <https://www.sciencedirect.com/science/article/pii/S0167610517304774>.
- Tabrizi, A.B., Whale, J., Lyons, T., Urmee, T., 2015. Extent to which international wind turbine design standard, IEC 61400-2 is valid for a rooftop wind installation. *J. Wind Eng. Ind. Aerodyn.* 139, 50–61. <http://dx.doi.org/10.1016/j.jweia.2015.01.006>, Retrieved from <https://www.sciencedirect.com/science/article/pii/S016761051500015X>.
- Toja-Silva, F., Kono, T., Peralta, C., Lopez-Garcia, O., Chen, J., 2018. A review of computational fluid dynamics (CFD) simulations of the wind flow around buildings for urban wind energy exploitation. *J. Wind Eng. Ind. Aerodyn.* 180, 66–87. <http://dx.doi.org/10.1016/j.jweia.2018.07.010>, Retrieved from <https://www.sciencedirect.com/science/article/pii/S0167610518302277>.
- Toja-Silva, F., Peralta, C., Lopez-Garcia, O., Navarro, J., Cruz, I., 2015. On roof geometry for urban wind energy exploitation in high-rise buildings. *computation* 3 (2), 299–325. <http://dx.doi.org/10.3390/computation3020299>, Retrieved from <https://www.mdpi.com/2079-3197/3/2/299>.
- Tolias, I., Koutsourakis, N., Hertwig, D., Eftimiou, G., Venetsanos, A., Bartzis, J., 2018. Large Eddy Simulation study on the structure of turbulent flow in a complex city. *J. Wind Eng. Ind. Aerodyn.* 177, 101–116. <http://dx.doi.org/10.1016/j.jweia.2018.03.017>, Retrieved from <https://www.sciencedirect.com/science/article/pii/S0167610517309765>.

- Tominaga, Y., Mochida, A., Yoshie, R., Kataoka, H., Nozu, T., Yoshikawa, M., Shirasawa, T., 2008. AJ guidelines for practical applications of CFD to pedestrian wind environment around buildings. *J. Wind Eng. Ind. Aerodyn.* 96 (10), 1749–1761. <http://dx.doi.org/10.1016/j.jweia.2008.02.058>, Retrieved from <https://www.sciencedirect.com/science/article/pii/S0167610508000445>.
- Veers, P.S., 1988. Three-dimensional Wind Simulation. Technical Report SAND-88-0152C, Sandia National Labs., Albuquerque, NM (USA), <https://www.osti.gov/biblio/6633902>.
- Vita, G., 2020. *The Effect of Turbulence in the Built Environment on Wind Turbine Aerodynamics (Doctoral Thesis)* (Ph.D. thesis). University of Birmingham.
- Vita, G., Hashmi, S.A., Salvadori, S., Hemida, H., Baniotopoulos, C., 2020a. Role of inflow turbulence and surrounding buildings on large eddy simulations of urban wind energy. *Energies* 13 (19), 5208. <http://dx.doi.org/10.3390/en13195208>.
- Vita, G., Salvadori, S., Misul, D.A., Hemida, H., 2020b. Effects of inflow condition on RANS and LES predictions of the flow around a high-rise building. *Fluids* 5 (4), 233. <http://dx.doi.org/10.3390/fluids5040233>.
- Vita, G., Šarkić-Glumac, A., Hemida, H., Salvadori, S., Baniotopoulos, C., 2020c. On the wind energy resource above high-rise buildings. *Energies* 13 (14), <http://dx.doi.org/10.3390/en13143641>.
- Vranešević, K.K., Vita, G., Bordas, S.P., Šarkić Glumac, A., 2022. Furthering knowledge on the flow pattern around high-rise buildings: LES investigation of the wind energy potential. *J. Wind Eng. Ind. Aerodyn.* 226, 105029. <http://dx.doi.org/10.1016/j.jweia.2022.105029>.
- Wyngaard, J.C., 2010. *Turbulence in the Atmosphere*. Cambridge University Press.
- Yakhot, A., Liu, H., Nikitin, N., 2006. Turbulent flow around a wall-mounted cube: A direct numerical simulation. *Int J. Heat Fluid Flow* 27 (6), 994–1009. <http://dx.doi.org/10.1016/j.ijheatfluidflow.2006.02.026>, Retrieved from <https://www.sciencedirect.com/science/article/pii/S0142727X06000476>.
- Yeow, T.S., Cuerva, A., Pérez-Álvarez, J., 2011. Pressure Measurements of the Detachment Bubble on the Bolund Island. In: *Proceedings of PHYSMOD2011 – International Workshop on Physical Modeling of Flow and Dispersion Phenomena*. University of Hamburg, Germany.